Materials Today Bio 29 (2024) 101356

Contents lists available at ScienceDirect

Materials Today Bio

journal homepage: www.journals.elsevier.com/materials-today-bio

A three-phase strategy of bionic drug reservoir scaffold by 3D printing and layer-by-layer modification for chronic relapse management in traumatic osteomyelitis

Yutong Zhang [a], Tongtong Xu [b], Tieshu Li [a,c,d], Hening Chen [a], Guangzhe Xu [c], Wenxin Hu [a], Yongting Li [a], Yue Dong [a], Zhihui Liu [b,**], Bing Han [a,*]

[a] School of Pharmaceutical Sciences, Jilin University, Changchun, 130021, China
[b] Department of Prosthodontics, Hospital of Stomatology, Jilin University, Changchun, 130021, China
[c] Changchun University of Chinese Medicine, Changchun, 130117, China
[d] Affiliated Hospital of Yangzhou University, Yangzhou, 225009, China

A B S T R A C T

We have developed a novel three-phase strategy for osteomyelitis treatment, structured into three distinct phases: the "strong antimicrobial" phase, the "monitoring and osteogenesis" phase and the "bone repair" phase. To implement this staged therapeutic strategy, we engineered a bionic drug reservoir scaffold carrying a dual-drug combination of antimicrobial peptides (AMPs) and simvastatin (SV). The scaffold integrated a bilayer gel drug-carrying structure, based on an induced membrane and combined with a 3D-printed rigid bone graft using a layer-by-layer modification strategy. The mechanical strength of the composite scaffold (73.40 ± 22.44 MPa) is comparable to that of cancellous bone. This scaffold enables controlled, sequential drug release through a spatial structure design and nanoparticle drug-carrying strategy. AMPs are released rapidly, with the release efficiency of 74.90 ± 8.19 % at 14 days (pH = 7.2), thus enabling rapid antimicrobial therapy. Meanwhile, SV is released over a prolonged period, with a release efficiency of 98.98 ± 0.05 % over 40 days in vitro simulations, promoting sustained osteogenesis and facilitating the treatment of intracellular infections by activating macrophage extracellular traps (METs). The antimicrobial, osteogenic and immunomodulatory effects of the scaffolds were verified through in vitro and in vivo experiments. It was demonstrated that composite scaffolds were able to combat the chronic recurrence of osteomyelitis after debridement, by providing rapid sterilization, stimulating METs formation, and supporting osteogenic repair.

1. Introduction

Traumatic osteomyelitis is a significant complication of infectious bone disease, presenting a considerable challenge in bone repair and regeneration [1]. Factors such as elevated body mass index (BMI), an ageing population and menopause-related bone loss increase the risk of wound infection and delayed bone healing [2], further complicating the management of this condition. Conventional treatment, typically involving antibiotics, is limited by theirfixed antimicrobial spectrum and poor penetration through cell membranes. These limitations hinder the eradication of intracellular infections is entirely difficult, which can result in immune dysfunction and the colonization of latent bacterial flora, leading to the chronic progression of osteomyelitis. Chronic osteomyelitis can persistently affect open wounds, causing prolonged pain and recurrent infections, eventually contributing to graft failure or systemic complications [3].

Simvastatin (SV), used to lower cholesterol as a competitive inhibitor of HMG-CoA reductase in clinical practice [4], is increasingly being investigated for its broader therapeutic potential. SV has been demonstrated to facilitate osteogenic mineralization by upregulating bone morphogenetic protein-2 (BMP-2), alkaline phosphatase (ALP) and osteogenic-related proteins [5]. In addition, SV has angiogenic, immunomodulatory and anti-inflammatory and antibacterial properties [6]. In our study, we discovered that SV can act as a regulator of macrophage traps, stimulating macrophages to produce nets-like structures, known as macrophage extracellular traps (METs), which works in conjunction with other antimicrobial components produced by the body's immune system to trap invading bacteria and prevent them from persisting within the cell by lysing both themselves and the bacteria [7].

Antimicrobial peptides (AMPs) represent a significant element of antimicrobial immunotherapy [8], which can rapidly remove bacteria and disrupt biofilm formation [9]. Antimicrobial peptides, mostly derived from the body's defense system, exhibit broad-spectrum antimicrobial activity. By disrupting bacterial membranes through

* Corresponding author.
** Corresponding author.
E-mail addresses: liu_zh@jlu.edu.cn (Z. Liu), hanb@jlu.edu.cn (B. Han).

https://doi.org/10.1016/j.mtbio.2024.101356
Received 11 June 2024; Received in revised form 11 November 2024; Accepted 21 November 2024
Available online 23 November 2024

electrostatic interactions, AMPs not only eliminate bacteria but also reduce neutrophil depletion, thereby modulating immune responses to enhance infection clearance.

Current strategies for treating traumatic osteomyelitis remain a lot of challenges. In practice, Masquelet's induced membrane technique (MIMT) has been demonstrated to facilitate bone reconstruction. However, it often requires secondary surgery, which can increase the overall treatment burden [10]. Furthermore, clinical strategies to prevent the recurrence of chronic osteomyelitis may involve the administration of high-dose intravenous antibiotics in conjunction with oral therapy for several weeks [11]. Nevertheless, prolonged antibiotic therapy may result in the emergence of drug-resistant bacterial strains, limiting the efficacy of conventional therapies [12]. The issue of the low metabolic activity of the latent bacteria has not been addressed. Intravenous infusions, chronic diseases, and surgical implantation may render the host immunodeficient, thereby allowing the bacteria to invade the immune defence system and disrupt the body's normal immune function, ultimately resulting in graft failure [13].

To address these issues, we have developed a novel dual-drug reservoir scaffold, designated Composite@AMPs/SV, to facilitate staged treatment of traumatic osteomyelitis. The scaffold consists of a 3D-printed PLA-mPEG rigid framework combined with a bionic induced membrane structure made from bilayer gels. The outer gel layer, composed of AMPs encapsulated in hyaluronic acid methacrylate (AMPs@HAMA), is designed to rapidly release antimicrobial peptides, while the inner gel layer, consisting of GelMA@PDA@PLGA loaded with simvastatin (SV), provides sustained release to promote osteogenesis and modulate immune responses. This spatial delineation of the soft tissue and the cavity ensures the attachment of osteoblasts [14]. Composite scaffolds are employed in the staged treatment of traumatic osteomyelitis through the delivery of drugs based on nanoparticles (NPs) and a layered degradation strategy utilizing a layer-by-layer modification system. During the initial stage of implantation, planktonic flora rapidly colonize the surface of the implanted material and form a biofilm [13], which can imped neutrophil penetration, resulting in neutrophil depletion through aberrant formation of NETs [15]. To reduce bacterial colonization and prevent biofilm formation, the outer ionogel AMPs@HAMA system accelerates the release of antimicrobial peptides, enhancing the initial antibacterial response. Following implantation, macrophages act as a vital link in the host's immune system, monitoring and clearing bacterial colonies [16] via a phagocytic process [17]. Nevertheless, phagocytosed bacteria may persist in a latent state within the host cell through the 'Trojan horse' effect [18]. The GelMA@PDA@PLGA/SV gel layer regulates phagocytosis and lysis by macrophages, preventing latent intracellular bacteria from affecting osteomineralisation and bone loss, which ultimately may defend the chronic recurrence of osteomyelitis. Furthermore, the inner gel facilitates osteogenic mineralization at the defect site through a sustained release strategy. The scaffolds were gradually transitioned from a high antibacterial strategy to a monitoring and osteogenic strategy through the utilisation of diverse release strategies involving SV and AMPs. This approach facilitated the clearance of intracellular infections and the induction of osteogenic regeneration, while reducing the invasive capacity of bacteria for osteoblasts and macrophages following scaffold action [15].

However, in the late stages of implantation, a balance of inflammation in the defect and successful osseointegration should be demonstrated, as chronic osteomyelitis may manifest itself as bone loss and failure of integration [19]. The osteogenic, antibacterial and anti-inflammatory functions of the scaffolds have been verified through both in vivo and in vitro experiments, demonstrating their potential for clinical application in the treatment of traumatic osteomyelitis.

2. Methods

2.1. 3D printed PLA-mPEG rigid scaffolds

A desktop 3D bioprinter (Sunp Biomaker Pro series, Sunp Biotech, Beijing, China) was used to fabricate 3D scaffolds in this study. The scaffolds were constructed layer by layer using computer-aided design/computer-aided manufacturing CAD/CAM technology. PLA-mPEG particles were loaded into a packing barrel and preheated at 75 °C for 30 min. Printing was conducted with a 400 μm diameter nozzle at a printing speed of 4 mm/s and an extrusion speed of 1 mm/s. After printing, the scaffolds were carefully removed from the platform, then sealed and stored under refrigeration [20].

2.2. Measurement of water contact angle

The wettability of the scaffolds was evaluated by measuring the contact angle of a 3 μL water droplet on the scaffold surface using a contact angle meter (Model CAM-MTCRO, Tantec). The droplet was imaged within the first 5 s using a high-speed video camera and the contact angle measurement system. This test was repeated three times for each scaffold, and the average value was reported [21].

2.3. Infrared spectroscopy

Fourier-transform infrared (FTIR, UMA-600 Microscope, Varian Excalibur Series) spectroscopy was used to determine the chemical composition and functional groups of the gel samples. Lyophilised gel samples were ground with a pulveriser and passed through a 200-mesh sieve. The FTIR analysis was then carried out on all the samples by mixing and grinding with 200 mg of KBr powder, then pressing into a transparent disc using a tablet press device. Spectra were recorded at wavelengths in the range of 600–4000 cm^{-1} with a resolution of 4 cm^{-1}. Finally, chemical bonds or functional groups were identified by analyzing spectral band wavelengths with Origin software [22].

2.4. Cell viability assay

Cells were inoculated into 24-well culture plates at a density of 5×10^5 cells per well. After 24 h of incubation, the medium was replaced with a medium containing each concentration group of drugs. After 3 days, the medium was discarded, and the cells were stained with Calcein-AM/PI staining solution, configured according to the instructions, and incubated in the dark for 15 min. Fluorescence images were captured with an inverted fluorescence microscope (Olympus CKX41, Tokyo, Japan). Fluorescence area was semi-quantitatively analyzed using ImageJ software.

2.5. Detection of cell surface viability

Cell viability on the surface of the scaffolds was assessed using the CCK-8 assay, with three replicates for each group. Scaffolds were placed in 24-well plates and seeded with 5×10^4 cells. On days 1, 3, and 5, the scaffolds were treated with Cell Counting Kit-8 reagent and incubated at 37 °C for 2 h. Absorbance at 450 nm was measured using an enzyme reader. All operations were performed in accordance with the kit specifications and performed in the dark.

2.6. ALP staining

ALP staining was performed using the azo-coupled staining method, with each group tested in six replicates. MC3T3-E1 cells were inoculated in 24-well plates and cultured in a 37 °C, 5 % CO2 incubator. Cells were then replaced with osteogenic differentiation medium containing 10 % FBS, L-ascorbic acid (50 μg/mL), and β-glycerophosphoric acid disodium salt (10 mM). On days 3, 7, and 14, cells were rinsed in PBS, fixed

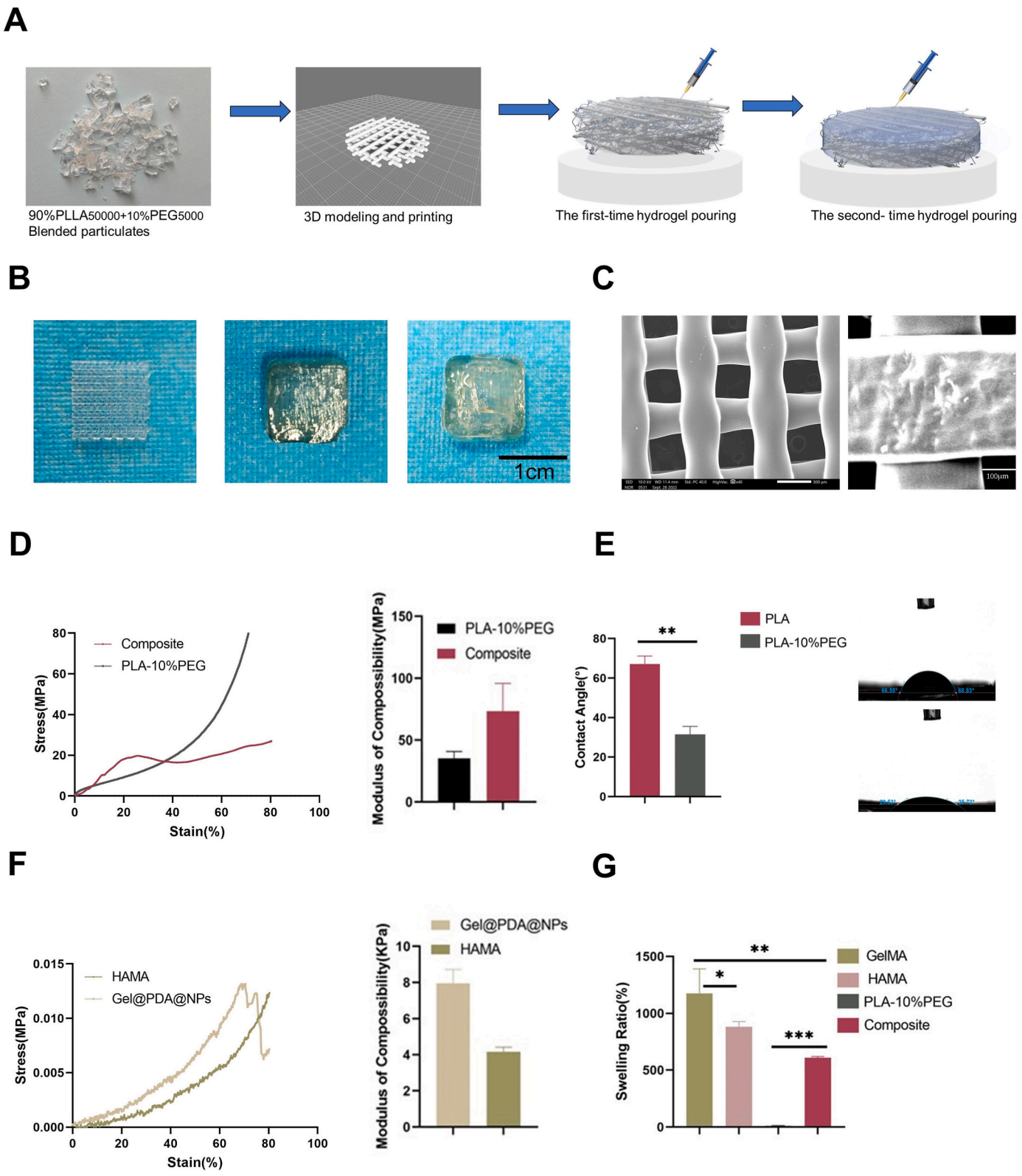

Fig. 1. Design, synthesis, and characterisation of composite scaffolds. (A). Design scheme of AMPs@HAMA/GelMA@PDA@PLGA/SV/PLA-mPEG composite scaffold (B). Physical images of the scaffold from left to right, PLA-mPEG,GelMA@PDA@PLGA/SV/PLA-mPEG, AMPs@HAMA/GelMA@PDA@PLGA/SV/PLA-mPEG (C). SEM images of 3D printed PLA-mPEG scaffolds (Scale bars = 500 μm and 100 μm, respectively) (D). Stress-strain curves, compression modulus of composite scaffolds and PLA-mPEG scaffolds (E). Water contact angle measurements before and after modification of 3D printed scaffolds (F). Stress-strain curves and compression modulus of gel (G). Swelling Ratio (Statistical significance: *$p < 0.05$, **$p < 0.01$, ***$p < 0.001$).

with 4 % (v/v) paraformaldehyde for 30 min, and stained with ALP staining solution according to the kit instructions in a dark environment. ALP activity was quantified from cell lysate supernatant at 520 nm using an enzyme marker [23].

2.7. AR staining

The experiments were performed as described above. On days 14 and 21 after culture, cells were fixed in 4 % (v/v) paraformaldehyde and stained with alizarin red (AR) according to the kit standard. Microscopy observation was conducted, and cells were lysed with TritonX-100, and the AR product was examined at 540 nm [24].

2.8. Determination of bacterial viability

Five groups of samples were immersed in 500 μL of bacterial suspension containing colony-forming units per milliliter (10^6 CFU/mL). After 2 h, samples were stained with a live/dead bacterial stain kit in the dark for 15 min. Dead bacteria stained red with the PI probe, and live bacteria labelled as green by the SYTO-9 probe. The observation was carried out using a confocal fluorescence microscopy.

2.9. Intracellular bacterial recovery

Scaffold extracts from different time points were used to pre-stimulate MC3T3-E1 cells, RAW264.7 cells, and MC3T3-E1 cells co-culture system. A 1 ml bacterial solution (10^8 CFU/mL) was introduced into the two types of cells. After 0, 10, 30, 60, and 120 min, antibiotics were added to eliminate free extracellular bacteria. Cells were then collected by centrifugation at 12,000 r/min for 10 min at 4 °C, lysed, and washed three times before inoculating LB medium with the resulting solution. Bacterial counts were compared with non-pre-treated controls to assess intracellular bacterial clearance efficiency [25].

2.10. MET capture

Isolated *S. aureus* was labelled with fluorescent dye and then implanted into RAW264.7 cells pre-treated with scaffolds. After 30 min of incubation, cell nuclei were stained with DAPI. Fluorescence microscopy was used for observation [7].

2.11. Establishment of traumatic osteomyelitis model

All animals used in this experiment were purchased from Liaoning Changsheng Laboratory Animal Company. The Institutional Animal Care and Utilisation Committee of the School of Pharmacy, Jilin University approved all animal work (No. 20210059).

Male SD rats weighing 300–350 g were used to establish a model of traumatic cranial osteomyelitis. Anesthesia was administered via intraperitoneal pentobarbital injection. Circular 8-mm cranial defects were created at the midline of the parietal bone using dental cannula. A bacterial suspension (10^8 CFU/mL) was injected into a gelatin sponge to fill the defects, which were then filled with bone wax. After 4 weeks, the defect infection was examined by X-RAY and Micro-CT. The necrotic and diffuse tissues were removed from the infected area, and the scaffold was implanted. After the placement of the composite scaffolds at the bone defect, rats were euthanized for 4 and 8 weeks by cardiac perfusion under anesthesia.

2.12. Micro-CT examination

To evaluate bone repair, an Inveon Multi-Modality System (Siemens) scans were conducted, with biopsies collected at 2 and 6 weeks. Specimens were fixed in 4 % paraformaldehyde following the euthanasia of the rats at 4 and 8 weeks. Two-dimensional X-ray images were used to reconstruct the three-dimensional images. Analysis of region of interest (ROI), bone volume fraction (BV/TV), bone volume (BV), bone surface area (BS), trabecular number (Tb.N), trabecular thickness (Tb.Th), and trabecular separation (Tb.Sp) were performed with Inveon Research Workplace (Siemens) [24].

2.13. Immunohistochemical staining

Rat cranial specimens were decalcified, and stained with HE, Marschall's trichrome, and immunohistochemical (IHC). Primary antibodies used were ALP (1:20,000, 13365-1-AP, ProteinTech, Wuhan, China), BMP-2 (1:20,000, 18933-1-AP, P-1), TNF-α (1: 400, GB11188, Servicebio, Wuhan, China), and CD31 (1:500, GB300604-H, Servicebio, Wuhan, China), with enzyme-labelled secondary antibody (1:20,000, 5220–0336, SeraCare, Beijing, China). Analysis of the stained area was conducted using ImageJ software.

2.14. Statistical analysis

Statistical analysis was performed using GraphPad Prism 8.0 software. Experimental data were first tested for Normality of Residual using the D'Agostino-Pearson omnibus (K2) test, followed by an assessment of homogeneity of variance with the Brown-Forsythe test. Differences between groups were assessed using analysis of variance (ANOVA) followed by Tukey's multiple comparison tests or Student's t-test. For data with unequal variances or non-normal distribution, Welch's *t*-test or Kruskal-Wallis non-parametric test was used. All data were presented as mean ± standard. At least 3 parallel samples were tested at each time point. Asterisks indicate statistical significance levels: *, ** and ***and**** represent $p < 0.05$, $p < 0.01$ and $p < 0.001$and $p < 0.0001$, respectively [26].

3. Results and discussion

3.1. Physical characteristics of 3D bionic drug reservoir scaffolds

The composite scaffold was manufactured by combining a 3D printed structure with a custom-made PTFE mold. The reservoir gel was introduced into the outer layer twice after 3D printing (refer to Fig. 1A). It was uniformly wrapped around the outer layer of the scaffold. PDA was introduced into the inner layer of the gel, which appeared black upon initial loading. The exterior of the scaffold appeared as transparent gel during the second wrapping of the outer layer. The change in colour indicated the uniform loading of the gel, as shown in Fig. 1B. The design of the structure is modelled on a double-layered induction membrane that separates the soft tissue from the graft, avoiding secondary surgery and residual bacteria from the soft tissue adhering to the surface of the hard bone graft.

Poly (lactic acid) (PLA) is a widely used material in additive manufacturing due to its FDA-approved degradability for medical purposes [27]. As per the literature, a 10 % covalent blend of polyethylene glycol (PEG) was selected to reduce the 3D printing temperature [28]. This reduction in temperature helped to prevent loss or denaturation during the hot-melt printing process. The 3D printing process was carried out at a temperature of 75 °C, with a printing speed of 4 mm/s and an extrusion speed of 1 mm/s. The line spacing was set to 1 mm, which resulted in scaffolds with appropriate porosity, as demonstrated in Fig. 1C. The pore size of the scaffolds was approximately 500 μm. Scaffold surfaces exhibit rough structural properties. The layer-by-layer modification system depicted in Fig. 1C demonstrated that PEG modification improved the surface roughness of the 3D-printed scaffold. Furthermore, it demonstrated stronger adhesion to the gel layer. The hydrophilicity of the modified artificial bone implant was found to be improved regarding the water contact angle [29]. Specifically, it was observed that after covalently bonding the material with PEG, the water contact angle decreased from 67.09 ± 4.11° for the pure PLA material to 31.51 ± 4.08°, as shown in Fig. 1E. The hydrophilicity of a material can

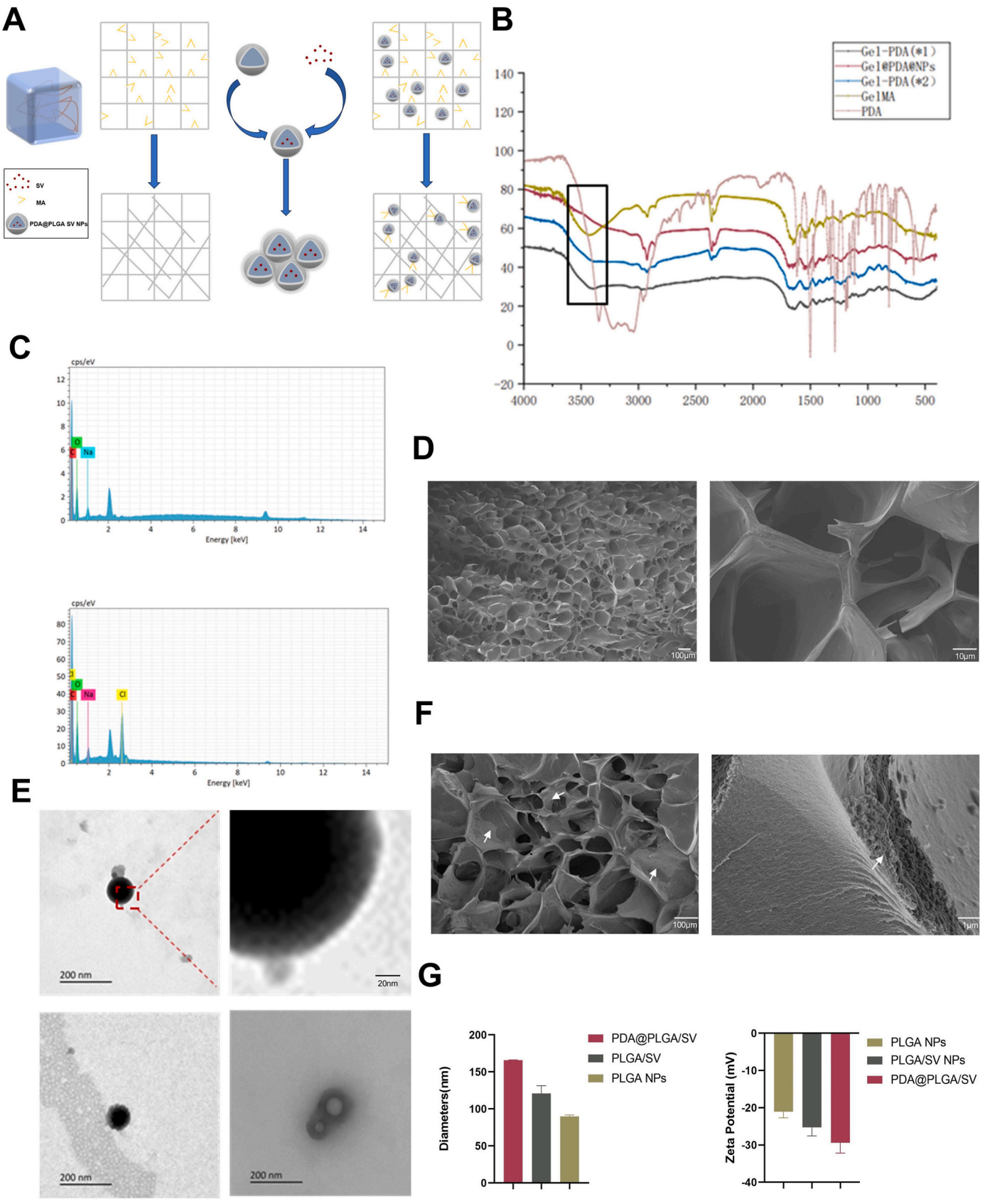

Fig. 2. The design and characterization of the GelMA@PDA@PLGA/SV gel layer. (A). Design scheme of GelMA@PDA@PLGA/SV gel system (B). FI-IR spectrogram (C). EDS energy spectrum (D). SEM micrograph of the gel (E). TEM micrographs and local magnification of PDA@PLGA/SV NPs, PLGA/SV NPs, TEM of PLGA NPs (G). Particle size and zeta potential of nanoparticles.

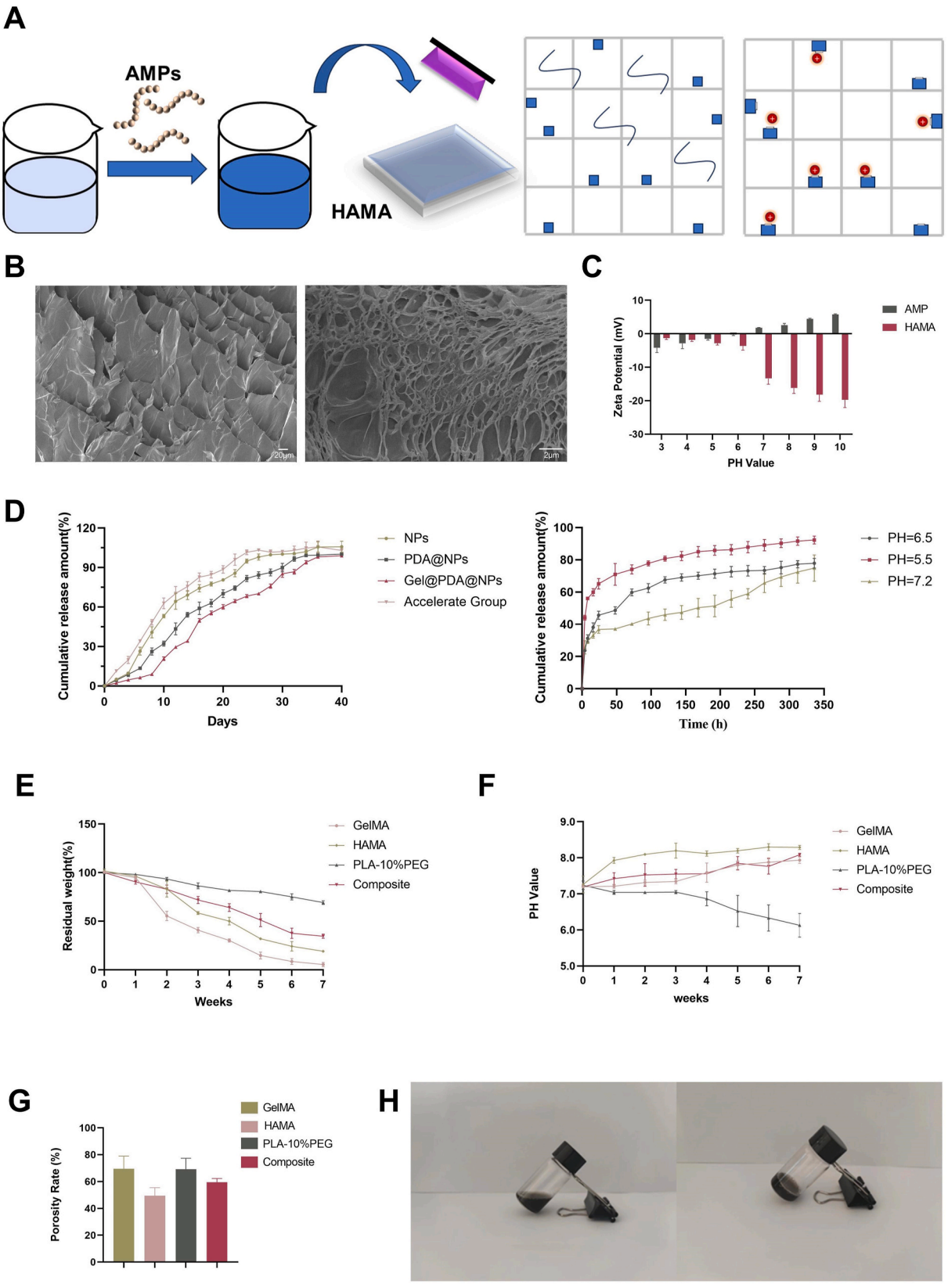

Fig. 3. Design and characterization of AMPs@HAMA gel layer, Overall evaluation of bilayer bionic gel layer. (A). Design scheme of AMPs@HAMA gel system (B). SEM micrographs of AMPs@HAMA gel layer (Scale bar = 20 μm and 200 μm) (C). Changes of zeta potential at different PH (D). Release profiles of SV in different systems, release profiles of AMPs at different PH (E). Degradation residual rate (F). Change in PH (G). Porosity (H). Gel formation of GelMA@PDA@PLGA/SV gels. (The data presented includes the standard deviation ± mean.)

be influenced by the water contact angle, which tends to be stronger when the angle is smaller. This phenomenon can be attributed to the increased intermolecular forces between the 3D-printed structure and the gel layer are greater, which results in a stronger bond between the two components. Supplementary Fig. S1 shows the changes in water contact angle for other modification materials in the layer-by-layer modification, while the adhesion of modification system was enhanced (Supplementary Fig. S3A). The study found that the mechanical level of composite scaffolds was enhanced. It was observed that the compression modulus of PLA-mPEG scaffolds was 35.20 ± 5.55 MPa. Although PEG modification decreased the mechanical strength of the scaffolds, it was still comparable to the strength of cancellous bone. The mechanical strengths of the Gel@PDA@NPs and HAMA scaffolds were 7.97 ± 0.76 KPa and 4.17 ± 0.25 KPa, respectively, as shown in Fig. 1F. It was also noted that PDA modification reduced the mechanical strength of the GelMA gel [30]. The GelMA mechanical strength was measured at 32.18 ± 3.02 KPa (Supplementary Fig. S2). Additionally, the composite scaffold was found to exhibit a compression modulus of 73.40 ± 22.44 MPa, which suggests an improvement in mechanical strength when compared to the gel system in Fig. 1F. The composite scaffold displayed a swelling rate of 608.78 ± 11.02 %, which was found to be intermediate between that of the GelMA gel (1175.38 ± 215.05 %) and the HAMA gel (881.69 ± 46.98 %) in Fig. 1G. The higher swelling rate of the gels is advantageous for drug storage, making the modified gel a suitable reservoir material.

The inner reservoir gels were used for in situ continuous delivery of SV. The design strategy for the inner reservoir gel is illustrated in Fig. 2A, which exhibits the binding of modifying groups and nanoparticles in the GelMA gel, as well as the alteration in the internal configuration of the gel under UV conditions. Three types of nanoparticles were prepared: PLGA NPs, PLGA/SV NPs, and PDA@PLGA/SV NPs. The average particle size of the nanoparticles was measured using dynamic light scattering, and their homogeneity was expressed as PDI, as shown in Fig. 2F. The three nanoparticles presented particle sizes of 89.80 ± 2.09 nm, 120.97 ± 10.44 nm, and 165.67 ± 0.67 nm, respectively, with PDI values of 0.215, 0.160, and 0.146. It is worth noting that all three nanoparticles had PDIs <0.3, which indicates good homogeneity [31]. The SV encapsulated nanoparticles were found to have a larger particle size compared to the empty nanoparticles. Furthermore, the addition of PDA resulted in a further increase in particle size. Both PLGA/SV NPs and PDA@PLGA/SV NPs nanoparticles had negative zeta potentials, indicating good stability of the nanoparticle dispersion system. The PDA modified nanoparticles exhibited enhanced electronegativity due to the presence of many dopamine oxidising catecholamine groups during dopamine oxidation [32]. The morphology and structure of various nanoparticles were observed using transmission electron microscopy, as shown in Fig. 2E. It was found that the modified nanoparticles exhibited a distinct core-shell structure, with the bare PLGA surface uniformly coated with PDA. The PDA coating, which is enriched with a variety of functional groups, is based on biologically inspired dopamine chemistry. Transmission electron microscopy revealed that the particle size of the nanoparticles was found to be smaller than that measured by dynamic light scattering. The aggregation and hydration of nanoparticles during dynamic light detection were taken into consideration [33]. PDA@PLGA/SV nanoparticles were incorporated into the gel network through PDA modification, resulting in a nanocomposite gel system. The GelMA gel was photocrosslinked using MA groups and 365 nm UV light. This mild chemical reaction has weak cytotoxicity but significantly enhances the gel's mechanical properties and extends its degradation time. The electron microscopy results showed that GelMA gel has a surface pore structure, but it is relatively smooth, which may promote bacterial adhesion and colonization, as illustrated in Fig. 2D. The modification of PDA couples the nanoparticles in the gel for secondary cross-linking. This occurs through intermolecular forces formed by the groups on the PDA and the GelMA groups, including hydrogen bonding and other forces. Hydrogen bonding is a non-covalent cross-linking force that facilitates the arrangement of PLGA/SV NPs in a double cross-linked network. It is important to note that this force is intermediate between chemical bonding and van der Waals forces. The PDA@PLGA/SV NPs have been incorporated into the gel system as a double cross-linked network, as detected by FI-IR (Fig. 2B). The amide I band group, which is a characteristic group of GelMA, broadens the spectral band at 3400 cm^{-1} and shifts towards the blue end of the infrared spectrum. The results indicate that the introduction of PDA directly into the GelMA system produces this change, and the broadening of the spectral bands is more pronounced as the concentration of PDA in the system is increased from 10 % to 20 %. It has been demonstrated that the introduction of PDA groups into the system produces a hydrogen bonding effect [33]. The same spectral band change was observed by introducing PDA-modified nanoparticles into the gel system, with the formation of broadband absorption peaks [22]. The results of EDS energy spectra are shown in Fig. 2C. It can be observed that the introduction of dopamine hydrochloride (Supplementary Fig. S3B) into the double-crosslinked system resulted in the incorporation of Cl element into the gel network, demonstrating the successful implementation of a mussel-inspired strategy in the gel network. Nanoparticles could potentially be coupled within the gel network using PDA and crosslinked with light to form a double-crosslinked network. This network may be ordered within the gel to enable controlled drug release [33]. Fig. 2D displays the morphology of the GelMA/PDA@PLGA/SV NPs double-crosslinked gel system as observed through electron microscopy. The surface of the gel appeared rougher, and the gel exhibited a loose and porous structural state, which is conducive to cell adhesion and proliferation. Supplementary data indicated that PDA modification increased hydrophilicity and adherence. Furthermore, PDA modification altered the gel colour, as shown in Fig. 3H, and extended the photocrosslinking time [34]. The GelMA/PDA@PLGA/SV NPs undergo a mussel-inspired layer-by-layer modification process to create a transition layer, which enhances the adhesion of the NPs. This, in turn, facilitates the tight linking of the three-layered structure. The drug is coupled in a gel network using the PDA@PLGA modification strategy, which prolongs the duration of action of SV, promoting osteogenesis and monitoring bacterial clearance in vivo. An examination was conducted of the in vitro release results of SV. The inner reservoir gel was able to prolong the release of SV and avoid the abrupt release effect. The encapsulation of NPs, modification of PDA and creation of binary formulation forms have all served to prolong the release of SV. In vitro, the Gel@PDA@NPs demonstrated a release efficiency of 98.98 ± 0.05 % over a 40-day release period; the release efficiency of PDA@NPs at 36 days was 99.48 ± 0.16 %; The release efficiency of NPs alone was 97.98 ± 1.90 % at 26 days, and all three formulation forms exhibited a long-time release pattern. The mechanism of PDA coating is a highly adsorbent coating material that can adhere to the surface of nanoparticles and fill in the colloidal interstitial space. This allows for drug-carrying nanoparticles to be integrated into the gel network through the PDA coating [35]. The controllability of the system is impacted by the conversion of photothermal effect by PDA, as well as the specific glass transition temperature (Tg) of PLGA, which affects the release efficiency of PLGA NPs. The controlled release of SV can be accelerated by the photothermal conversion effectiveness of PDA, and in the face of difficult to remove infections, the system can be accelerated by the accelerated release system to improve the release efficiency of the system [36].

The outer gel reservoir stores antimicrobial peptides through charge attraction, which is based on pH adjustment (refer to Fig. 3A). AMPs (HHC-36) are cationic polypeptides with amphoteric ionization properties and are affected by the pH of the system, resulting in a different charge. Fig. 3A illustrates the occurrence of electrostatic gravitational forces between the two. The measurement of the potential of AMPs at different pH values indicates that AMPs tend to carry a positive charge when the pH is above 6. In physiological conditions, at pH 7.2, AMPs can interact with the bacterial cell membrane through both positive and

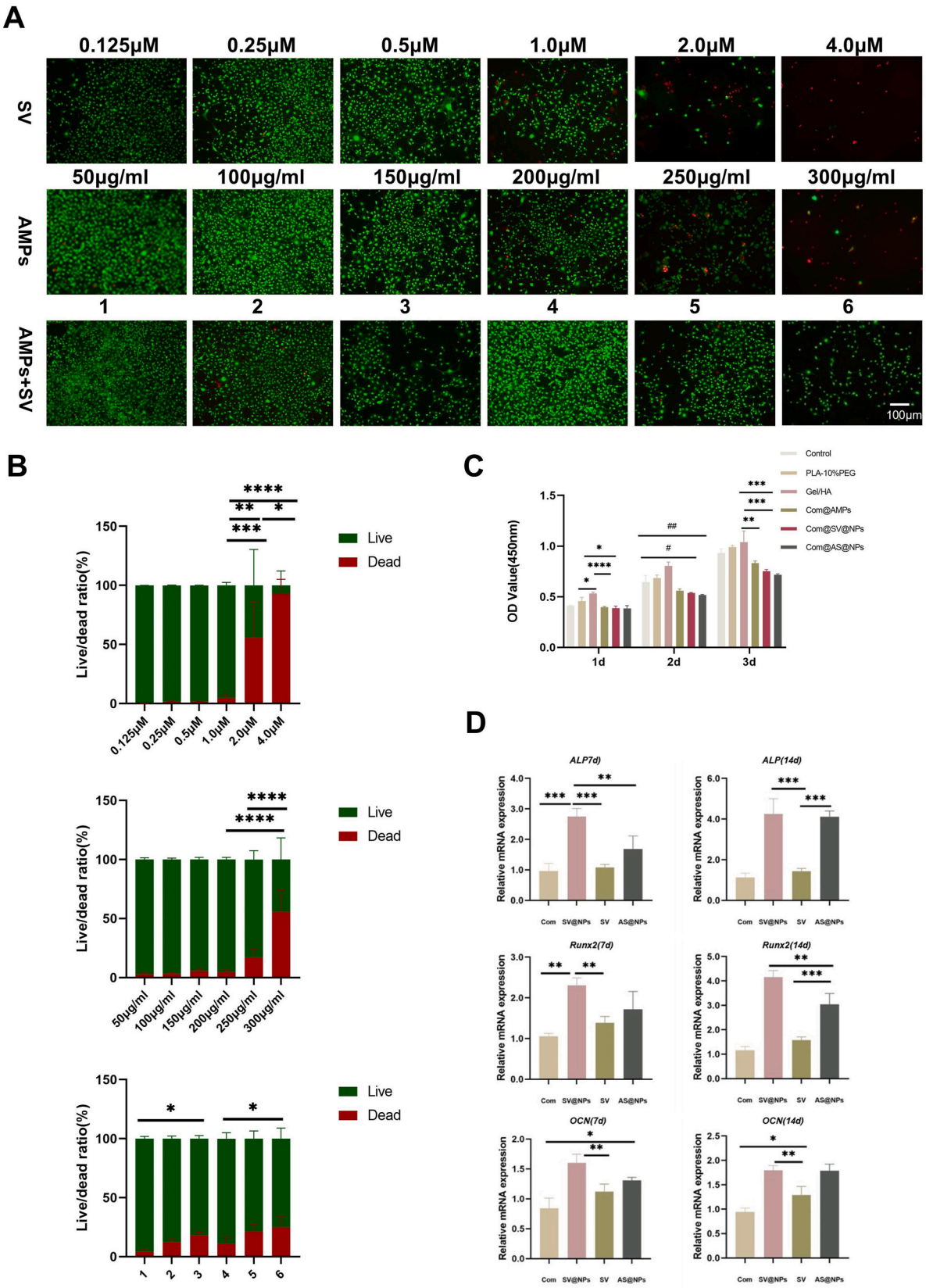

Fig. 4. Effect of the composite scaffold system with dual drug combination on MC3T3-E1 cells in vitro. (A). Dose screening of SV, AMPs, and combined drug groups (Scale bar = 100 μm) (B). Quantitative results of live-dead fluorescence (C). Cell proliferation on the surface of different groups of scaffolds (n = 3) (D). Osteogenic gene expression levels in MC3T3-E1 cells (The statistical significance of the results is indicated by the symbols: $^{\#}p < 0.05$ vs. control, $^{\#\#}p < 0.01$ vs. control, $^{*}p < 0.05$, $^{**}p < 0.01$, $^{***}p < 0.001$, $^{****}p < 0.0001$).

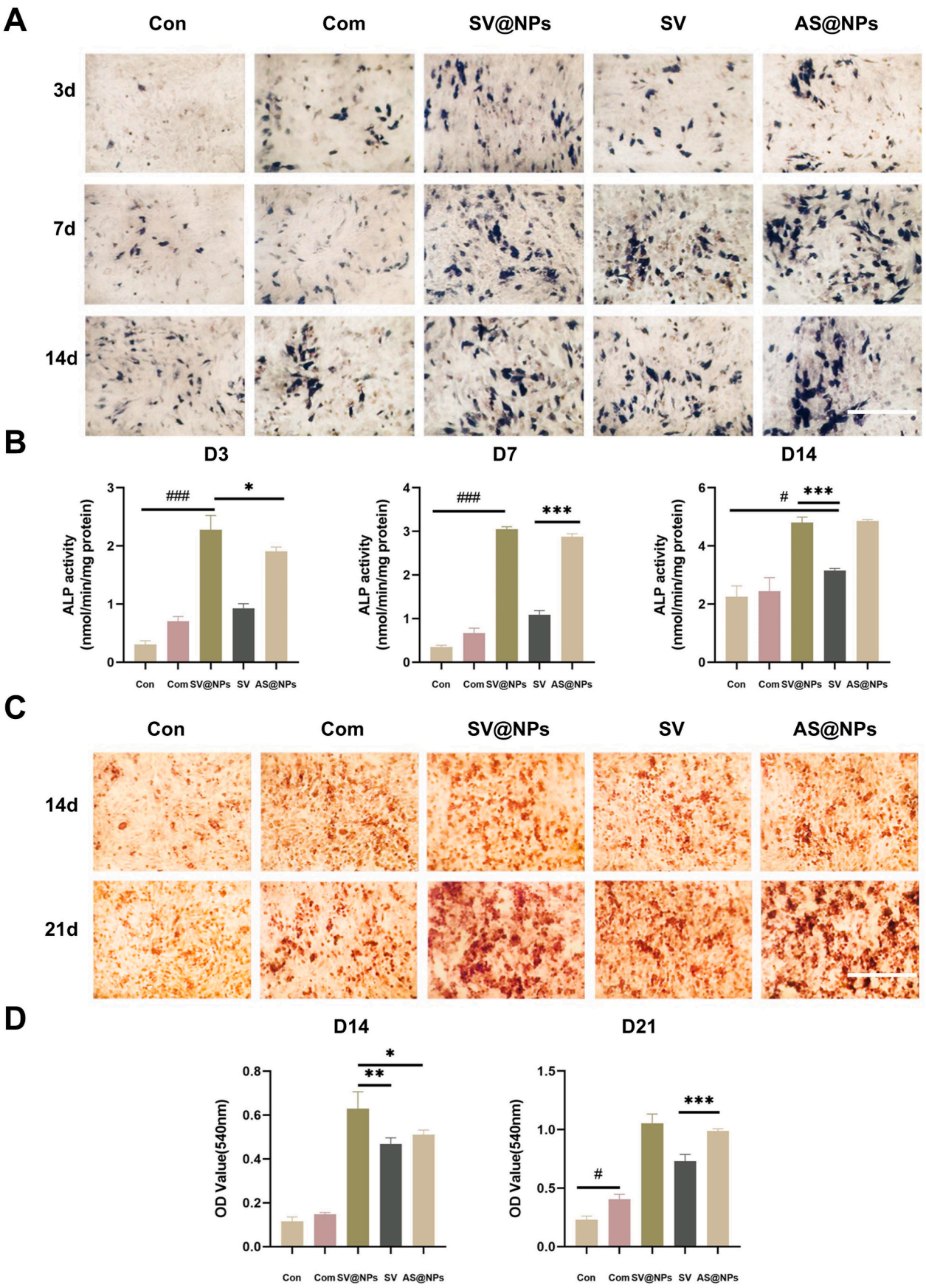

Fig. 5. Evaluation of in vitro osteogenic effects of composite scaffold systems. (A). ALP staining (Scale bar = 200 μm) (B). Quantitative analysis of ALP(C). AR staining (Scale bar = 200 μm) (D). Quantitative analysis of AR (The statistical significance of the results is indicated by the symbols: $^{\#}p < 0.05$ vs. control, $^{\#\#}p < 0.01$ vs. control, $^{\#\#\#}p < 0.001$ vs. control, $^{*}p < 0.05$, $^{**}p < 0.01$, $^{***}p < 0.001$).

negative charges. This interaction may cause membrane disruption, ultimately resulting in bacterial death [37]. Hyaluronic acid is a negatively charged polysaccharide and its electronegativity tends to increase with increasing pH [38]. At pH 10, it is observed that the gel and the drug have opposite charges in Fig. 3C, which facilitates the adsorption of the drug into the gel by electrostatic attraction, and then the gel is cross-linked a second time by the MA groups to form an ionic composite gel system. The AMPs@HAMA system formed at pH 10 responds to the acidic environment. This promotes the separation of gel and drug. As acidic metabolites are produced after bacterial infection, we simulated the release profiles of ionic gels PH = 5.5, PH = 6.5 and PH = 7.2 in vitro, see Fig. 3D, the AMPs@HAMA system maintains the highest release efficiency at PH = 5.5, with an average release efficiency of 92.33 ± 2.4 % after 14 days, this suggests that the drug reservoir gels are capable of rapidly releasing AMPs under pathological conditions. It has been demonstrated that the drug reservoir gels are capable of rapidly releasing AMPs under pathological conditions. Implantation and surgical procedures can be high risk areas for bacterial introduction [39], and the rapid release of the AMPs prevents biofilm formation on the implant surface. Release under specific pH conditions reduces toxic effects on cells. The AMPs@HAMA system was chosen as the gel reservoir, HAMA has a relatively dense structure, the outer layer is relatively rough, showing fish scale-like layering, see Fig. 3B, the dense structure protects the peptide drugs stored in the drug carrier system from hydrolysis by proteases, and the rough surface avoids bacterial adhesion and colonization As illustrated in Fig. 3D, the layered structure of the composite system effectively retards the degradation of the inner gel, resulting in a markedly longer degradation period compared to the pure gel system. In comparison to AMPs, SV exhibited a longer release time [40]. The composite scaffold system effectively controls the spatial release of drugs through its layered design, resulting in a gradual transition from releasing more AMPs at the beginning to releasing mainly SV. This transition represents the shift of the composite scaffold from the 'strong antimicrobial phase' to the 'surveillance and osteogenesis' phase. PLA-mPEG scaffolds produce acidic metabolites when metabolised, and the system PH drops to 6.13 ± 0.3. Our PH-based induced ionic reservoir gel compensates for this by maintaining the pH during scaffold metabolism (see Fig. 3F). The rate of reservoir gel degradation is greater than that of bone graft scaffolds over the time range of our measurements (see Fig. 3E). Consequently, the pH of the composite system is on an increasing trend, creating a weakly alkaline environment that is conducive to osteogenesis and bacterial clearance [41].

3.2. Osteogenic effects of 3D bionic drug reservoir scaffolds in vitro

To prevent antimicrobial drug resistance and reduce the negative impact of drugs on osteogenesis, we confidently determined the optimal dose for the combination group based on its effect on osteoblasts. Simvastatin acts as a drug with a short half-life, poor water solubility, and high toxicity. Simvastatin induces an inflammatory response and inhibits cell proliferation at high concentrations. While at low concentrations, it has a weak osteogenesis-promoting effect and fails to induce production of the bone morphogenetic protein BMP-2 [42]. The critical concentration at which simvastatin produces toxic effects is 1μM. A series of concentration gradients was designed based on a reference dose and incubated with MC3T3-E1 cells for a period of three days (Fig. 4B). The data demonstrated a clear concentration-dependent relationship between SV concentration and cell proliferation inhibition. The study found that cell inhibition occurred at concentrations exceeding 1 μM of the drug, with an inhibition rate of 55.69 ± 30.4 % at 2 μM. Osteoblasts were significantly inhibited by 92.95 ± 12.2 % at 4 μM, clearly indicating that the concentration of simvastatin in the preparation of bionic drug-carrying scaffolds should not exceed 1μM. This study provides a valuable reference for selecting the appropriate SV concentration. AMPs should rapidly remove bacteria at reasonable concentrations without affecting the proliferation and differentiation of osteoblasts. To investigate the level of growth inhibition of osteoblasts, a series of concentration gradients were designed based on the IC50 (Supplementary Table S4) of AMPs. The experiment showed that drug concentrations of 50, 100, 150, and 200 μg/ml had a negligible inhibitory effect on cells. In contrast, at a concentration of 250 μg/ml, cell inhibition began to increase, and at 300 μg/ml, the level of cell inhibition reached a significant 55.68 ± 18.3 %. To prevent any negative impact on cell proliferation caused by the simultaneous action of two drugs, we conducted a co-application experiment. Two orthogonal experimental groups were established, each comprising three levels, based on the selected concentrations of AMPs and SV (Supplementary Table S3). Group 4 demonstrated excellent cell growth characteristics. The final concentration of SV was determined to be 0.8 μM and AMPs was 150 μg/ml, which was the concentration of the drug released in the bionic scaffolds (Fig. 4A). Osteoblasts were cultured on the scaffolds, and their cell growth on the surface was monitored using CCK-8 (as shown in Fig. 4C). The results demonstrated a proliferative trend over time, with the composite scaffold group without loaded drugs exhibiting the fastest rate of cell growth and proliferation on the surface. This indicates the scaffold's pro-proliferative efficacy and its capacity to facilitate cell adhesion. Notably, the release of screened groups of drugs in the scaffolds did not have a significant adverse effect on proliferation [31].

To treat osteomyelitis, it is crucial to assess the osteogenic capacity of the defect post-debridement. The osteogenic mineralization capacity of the composite scaffolds was evaluated by measuring the levels of alkaline phosphatase (ALP) and alizarin-stained calcium nodules (AR). Fig. 5A, B shows the results of alkaline phosphatase staining and quantitative analysis on days 3, 7 and 14, respectively. Alizarin staining and quantification were performed on days 14 and 21, as shown in Fig. 5C and D. The rational delivery format and sequential release in the composite group stimulate bone formation effectively. In contrast, the Composite@AMPs group is not effective in promoting bone formation (Supplementary Fig. S6). AMPs as antimicrobials, avoid the adverse effects of osteogenesis mainly through the sequential delivery system. Late composite scaffolds derive their osteogenic capacity mainly from the sustained SV release. We analyzed SV encapsulated in gel as a prototype drug, highlighting the significance of the composite drug delivery system in osteogenic mineralization. Furthermore, when SV is directly encapsulated in hydrogels, its insolubility results in the clogging of the pores of hydrogels, which is unfavorable for cell proliferation and adhesion on gels. (Supplementary Fig. S5). The study utilized *qRt-PCR* to examine the expression of genes related to osteogenesis, as shown in Fig. 4D. The results revealed the detection of key genes involved in the process of osteogenesis, including *ALP*, *Runx2*, and *OCN*. *ALP* is the earliest and most representative marker of osteogenesis. An increase in *ALP* indicates the initiation of osteogenesis. The composite delivery system significantly detected an increase in *ALP* expression level at 7 days. *Runx2* expressed in osteoblasts, has a significant impact on collagen production and calcification levels in these cells. Our delivery system has been shown to significantly increase the expression levels of *Runx2*, leading to increased osteogenic differentiation. Additionally, *OCN* (A hormone derived from osteoblasts and an important marker of late osteogenic differentiation) significantly increased at both 7 and 14 days, providing long-term regulation of osteogenic levels [43].

3.3. 3D bionic drug storage scaffolds for infection treatment in vitro

An in-vitro investigation was conducted to assess the antimicrobial capacity of the scaffold using *E. coli* and *S. aureus*. Recurrence after infection is a common complication in osteomyelitis. Research indicates that the number of colonies on the scaffold surface peaks during the initial period of implantation [44]. Prompt removal of bacteria is crucial to prevent the formation of biofilms, which are stationary colonies attached to the surface of the cytoplasmic matrix. It is noted that biofilms possess refractory properties in relation to planktonic colonies due

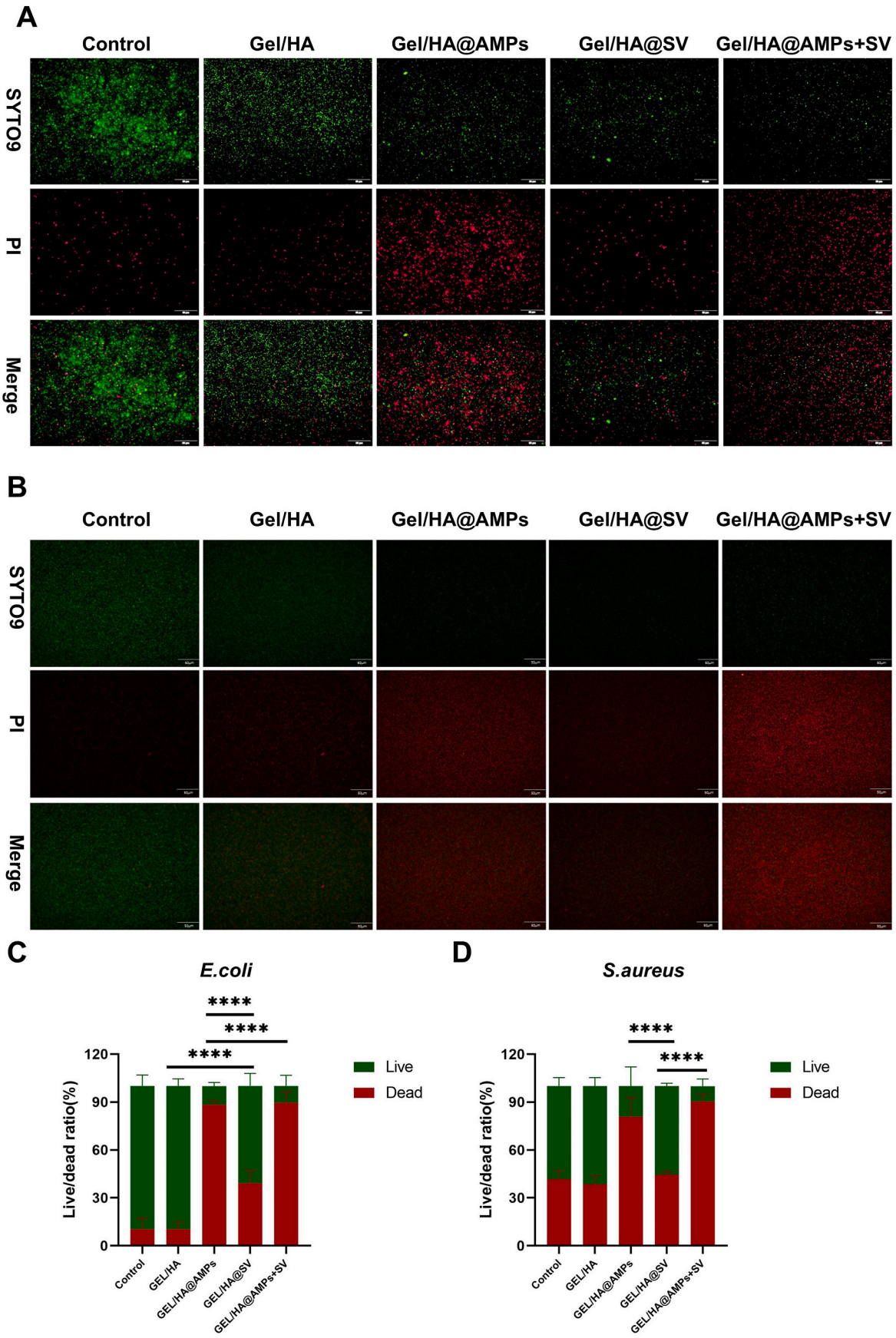

Fig. 6. In vitro antimicrobial evaluation of composite scaffold systems. (A). *E. coli* live-dead fluorescence staining (Scale bar = 50 μm) (B). *S. aureus* live-dead fluorescence staining (Scale bar = 50 μm) (C). Quantitative analysis of *E. coli* fluorescence (D). Quantitative analysis of *S. aureus* fluorescence (The statistical significance of the results is indicated by the symbols: *p < 0.05, **p < 0.01, ***p < 0.001, ****p < 0.0001).

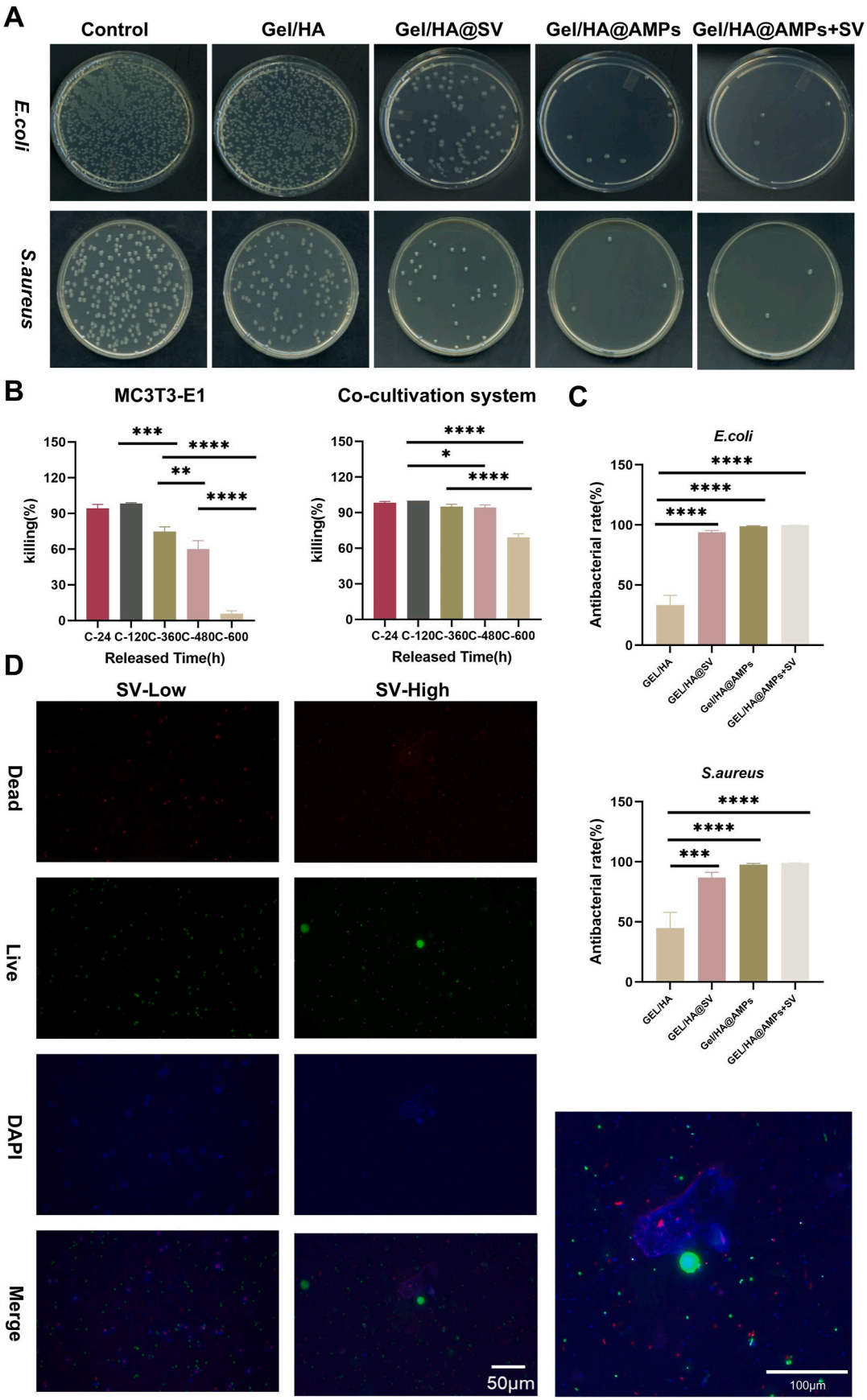

Fig. 7. In vitro antimicrobial evaluation and treatment of intracellular infections with composite scaffold (A). Colony forming unit (CFU) counts (B). Intracellular bacterial count (C). Quantitative results of CFU (D). MET fluorescence imaging (Scale bar = 50 μm and 100 μm) (The statistical significance of the results is indicated by the symbols: *p < 0.05, **p < 0.01, ***p < 0.001, ****p < 0.0001).

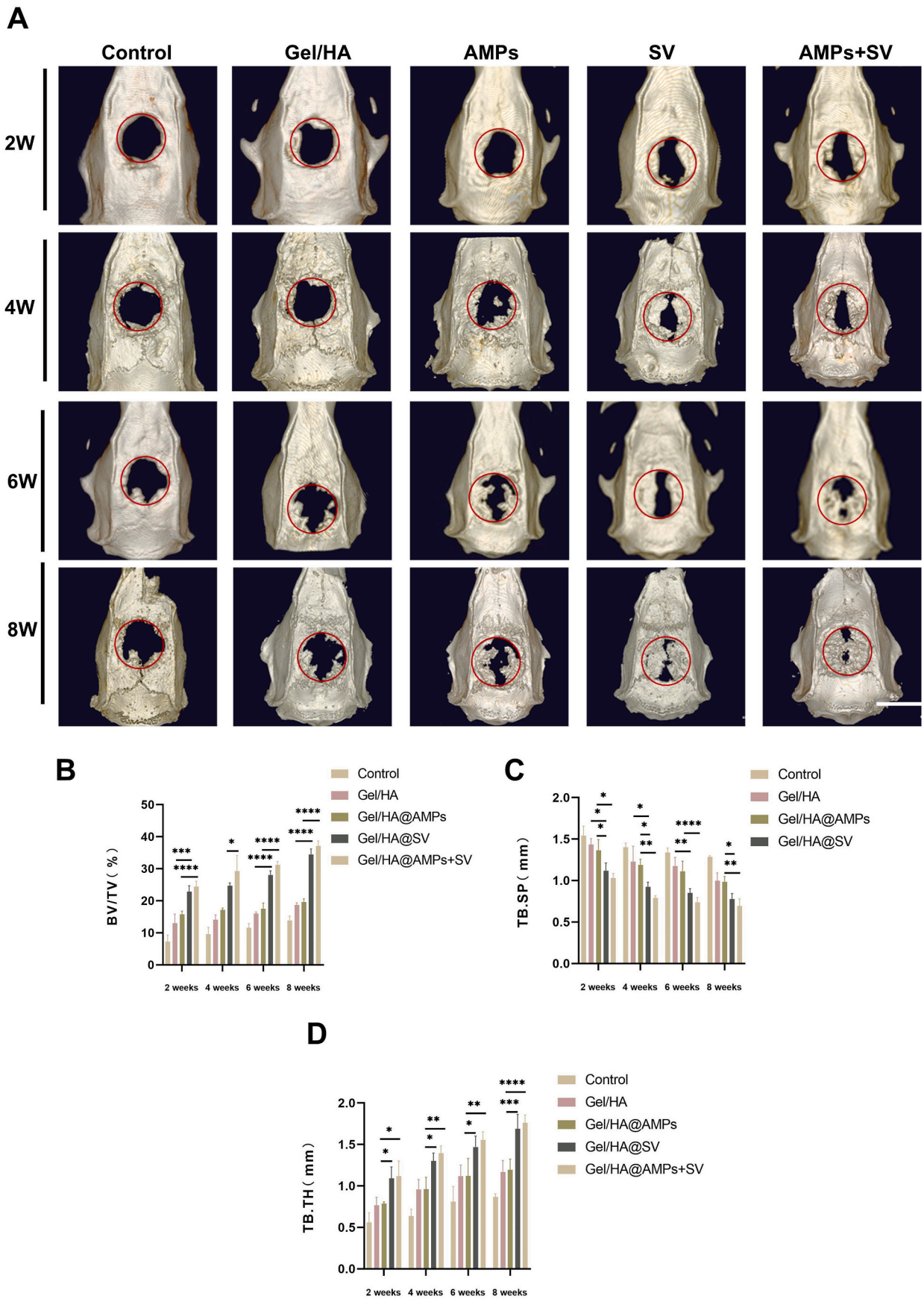

Fig. 8. In vivo osteogenic evaluation of composite scaffold systems (A). Micro-CT 3D reconstruction images at 2, 4, 6, and 8 weeks (Scale bar = 8 mm) (B) BV/TV (%) (C). TB. SP (mm) (D). TB. TH (mm) (The statistical significance of the results is indicated by the symbols: *p < 0.05, **p < 0.01, ***p < 0.001, ****p < 0.0001).

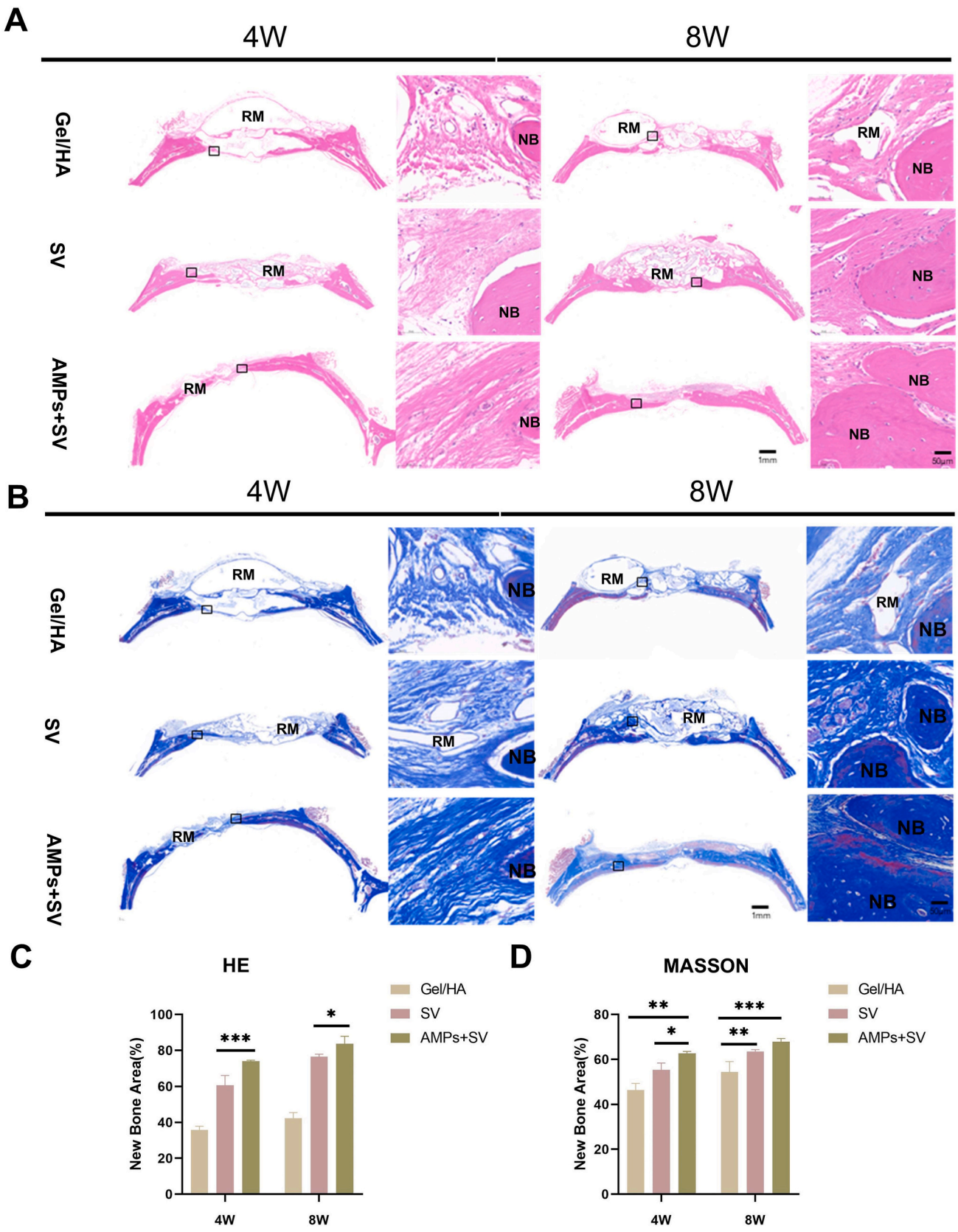

Fig. 9. Defect healing characteristics of different composite stent systems. (A). HE staining (B). MASSON staining (C). Quantitative analysis of HE(D). Quantitative analysis of MASSON (NB: new bone, RM: remaining materials. The scale bars at low magnification (× 1) and high magnification (× 40) are 1 mm and 50 μm, *$p < 0.05$, **$p < 0.01$, ***$p < 0.001$).

to effects such as group sensing [45]. The study utilized the AMPs (HHC-36) as a model drug and SV as a co-administration group. Prior research has established that SV not only enhances bone formation but also possesses antibacterial properties [42]. The study established an SV-accelerated release group. The surface of the drug-carrying nanoparticles was modified with PDA, which exhibits significant infrared responsiveness and photothermal conversion efficacy. The application of infrared irradiation has been demonstrated to accelerate the release process of SV, thereby offering a promising avenue for the treatment of severe and recurrent infections. AMPs eliminate bacteria by binding to negatively charged lipid membranes, disrupting their structure, and causing rapid death upon loss of the outer protective layer. They also prevent biofilm formation and dissolve pre-existing biofilms [46]. This study demonstrates that AMPs are highly effective in rapidly clearing bacterial infections associated with osteomyelitis (Supplementary Fig. S7). The antimicrobial drug is rapidly released through a double cross-linking network with a HAMA-based hydrogel that maintains excellent resistance to both strains of the bacterial organism. The study investigated the efficacy of the scaffolds against two strains of bacteria with different action times (Supplementary Fig. S8). The scaffold group with the addition of AMPs alone demonstrated an average antibacterial rate of 97.73 % against *S. aureus* and 98.95 % against *E. coli* after only 2 h of reaction, effectively inhibiting the in vitro formation of colonies compared to the control group (refer to Fig. 7A). The SV scaffold group demonstrated a level of in vitro inhibition, with 86.90 % and 93.77 % inhibition against two types of colonies, respectively. The results were comparable to those of the AMPs group ($P > 0.05$), indicating that SV is an effective bacterial inhibitor (refer to Fig. 7C). The experimental group that received IR-accelerated scaffold release showed a significantly higher antibacterial rate compared to the control group. These results suggest that IR light irradiation can effectively accelerate SV release, leading to synergistic antibacterial effects. Furthermore, we analyzed the stents in each group after incubating them with *S. aureus* and *E. coli* for 2 h. By utilizing a live/dead bacterial staining kit and fluorescence microscopy, as shown in Fig. 6, we were able to detect the number of dead and live bacteria.

The fluorescent staining results showed a consistent antimicrobial trend with increasing levels of antimicrobial activity in the SV, AMPs and accelerated release groups compared to the coated plate method.

The therapeutic effect of the Gel/HA@AMPs + SV dual-drug scaffold in preventing and treating intracellular infections in osteomyelitis recurrence was investigated in the study. The mechanism involves the generation of extracellular traps by macrophages. *S. aureus* invades macrophages and osteoblasts, resulting in intracellular infection. Invasion of osteoblasts leads to difficult bone healing and macrophage transformation as a 'Trojan horse' [47]. The scaffolds were selected based on their differing release profiles, with the release preferences of the two drugs in the in-scaffold combination group being switched. Osteoblasts were inoculated with the cells at a *S. aureus* ratio of 500:1. The number of colonies recovered from the cells was counted at different time points to evaluate therapeutic efficacy against intracellular infections (Supplementary Fig. S9).It was shown that the highest bacterial killing rate of 98.33 ± 0.6 % was observed in the Composite scaffold (C-120 h) group at 120 min of bacterial inoculation, and there was a decreasing trend of intracellular bacterial killing in the scaffold group after C-360 h, which was correlated with the decrease in the release of AMPs. However, the rate of intracellular bacterial killing in the C-600 h group was only 5.67 ± 2.5 %. Co-incubating macrophages and osteoblasts at a ratio of 1:1 significantly reduces the number of intracellular bacteria recovered during co-incubation. The bacterial killing rate at C-600 h was 69.00 ± 3.0 %, indicating that the clearance of intracellular infections by the scaffold is dependent on macrophages. (refer to Fig. 7B). To investigate the responsiveness of macrophages to bacteria after SV release, we implanted labelled bacteria into cells. We then labelled the nuclei of the cells and observed after 30 min. The observations made in the scaffold set of SV-High indicate that dead bacteria were dispersed around diffusely lysed nuclei. The nuclei lost their original morphology and were released to form a mesh around the bacterium, ultimately leading to its demise. Macrophages may aggregate viable bacteria, and attraction of viable bacteria to the reticulum were observed. The nuclear DNA of the macrophages kills the bacteria in a "homogeneous" form. The SV-Low scaffold set mostly shows intact nuclei, and the bacteria may be localized in the nucleus (refer to Fig. 7D).

Extracellular traps serve as an effective innate defense against bacterial immune clearance. However, it is important to note that sustaining a trap state may have adverse effects. For instance, macrophages may convert to pro-inflammatory genesis and secrete inflammatory factors. It is crucial to consider these potential consequences when utilizing extracellular traps as a defense mechanism [48]. PCR analysis determined that the expression of pro-inflammatory factors *TNF-α* and *IL-6* decreased, while the expression of anti-inflammatory factor *IL-10* increased. This suggests that low-dose delivery of SV can exert immunomodulatory effects (Supplementary Fig. S10).

3.4. Osteogenesis of 3D bionic drug reservoir scaffolds in rats with traumatic osteomyelitis in vivo

The study established an animal model of cranial osteomyelitis after debridement to evaluate composite scaffolds in vivo. The osteomyelitis infection was characterized by abscesses and localized bone dispersion [49]. Please refer to Supplementary Figs. S11 and S12for further details. The study demonstrates that the scaffolds used in the experiment were effective in promoting osteogenesis. Micro-CT was used to assess the osteogenesis of defects at 2, 4, 6, and 8 weeks after osteomyelitis debridement. It is worth noting that the 8-mm defect model exceeded the limit of critical osteogenesis and had low bone tissue healing without intervention [50]. However, new bone formation was observed in all scaffold groups. The scaffold for the drug reservoir facilitated a gradual release of SV, which was proven to be a highly effective promoter of both osteogenesis and angiogenesis. As a result, there was a significant increase in the production of new bones at the site of the defect. The Cel/HA@AMPs group effectively corrected the infected environment at the osteomyelitis when combined with SV, leading to timely promotion of osteogenesis. Furthermore, the software analysis revealed that implantation of scaffolds resulted in new bone regeneration, as evidenced by an increase in bone volume fraction (BV/TV), an expansion of trabecular thickness (Tb.Th), and a reduction in trabecular separation (Tb.Sp) [50]. The BV/TV (%) value of Cel/HA@AMPs + SV after 8 weeks was 37.15 ± 1.52 %, which was higher than the control group's value of 13.79 ± 1.43 % and the SV group's value of 34.46 ± 1.72 %.The BV/TV (%) value of the combination group was not significantly different from that of the SV group ($P > 0.05$), indicating that SV is the primary drug responsible for the osteogenic effects in the system. The trend of increased bone trabecular thickness was consistent with the BV/TV (%) value. The treatment led to increased new bone production, decreased trabecular separation, and an overall improvement in bone trabecular integrity. The combination group demonstrated the most significant improvement (refer to Fig. 8).

Histological observation using haematoxylin and eosin (HE) staining revealed that at four weeks, the reticular fibre arrangement was more tightly packed in the Cel/HA@ SV and Cel/HA@AMPs + SV groups compared to the control group. Local new bone generation was observed, and scaffolding residues were present upon sectioning (Fig. 9A–C).

Furthermore, the promotion of new bone generation was significantly more pronounced in the Cel/HA@AMPs + SV group, which was more tightly packed in fibrous tissues due to the rapid clearance of bacteria, thereby facilitating bone regeneration. At 8 weeks, all groups demonstrated a similar growth trend compared to 4 weeks, but with significantly higher bone gain. The scaffold exhibited remarkable capability for long-term osteogenesis in the defect, as evidenced by its

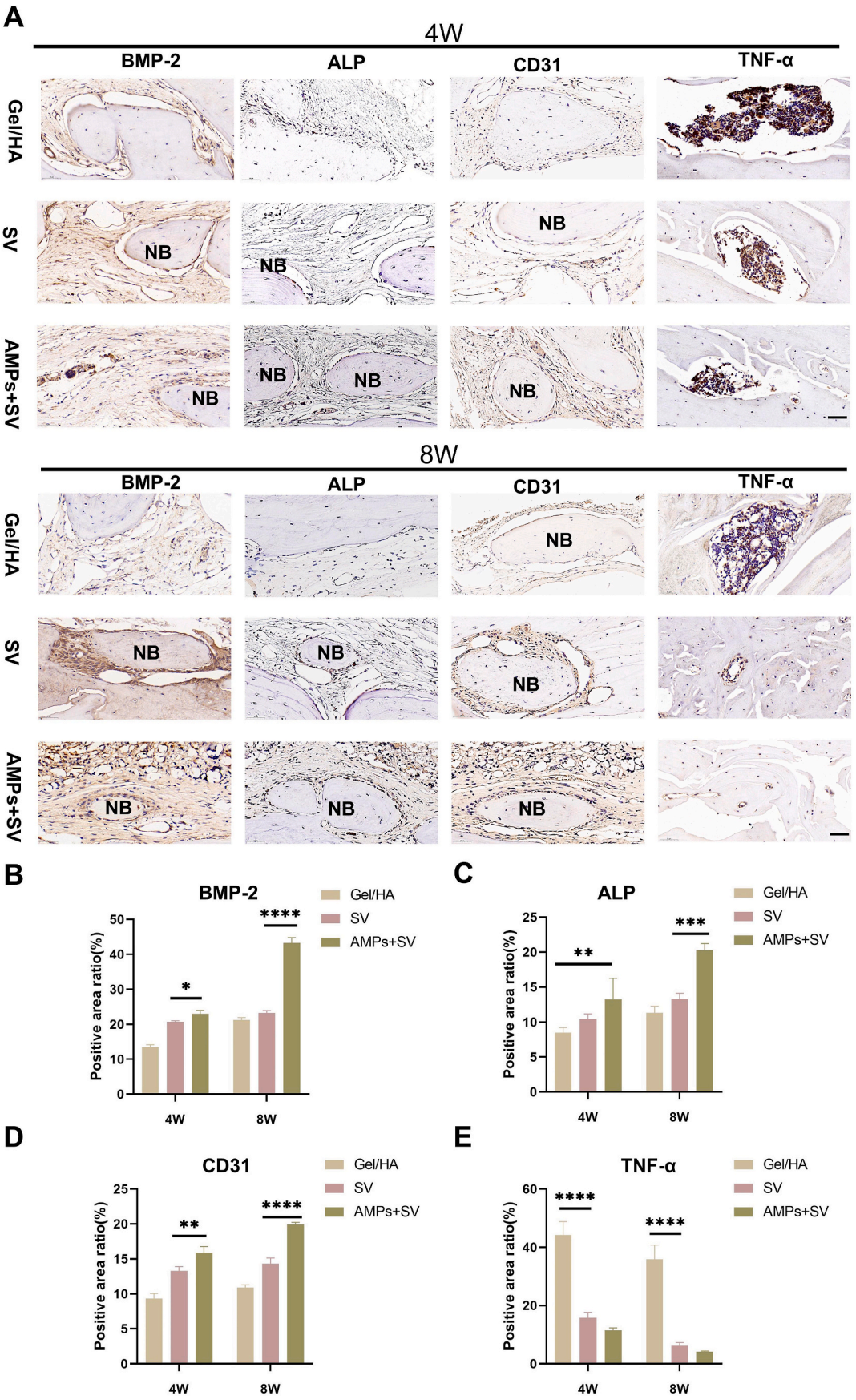

Fig. 10. Osteogenic, angiogenic and anti-inflammatory measurements of different composite scaffold systems. (A). Expression of, BMP-2, ALP, CD31, and TNF-α proteins in rat cranial bone. (Scale bar = 50 μm) (B). Quantitative analysis of BMP-2(C). Quantitative analysis of ALP, (D). Quantitative analysis of CD31 (E). Quantitative analysis of TNF-α. (NB: new bone; Scale bar = 50 μm; *p < 0.05, **p < 0.01, ***p < 0.001, ****p < 0.001).

partial integration into the skeletal tissue. Local magnification in the Cel/HA@AMPs + SV group clearly revealed the regeneration of collagen fibres around the scaffolds. This observation was confirmed by MASSON trichrome staining. In the dual-drug co-release group, the collagen fibres were more densely arranged, resulting in a significant increase in new osteogenesis. This demonstrates the remarkable facilitating effect of the dual-drug delivery system on bone treatment (Fig. 9B–D).

SV plays a therapeutic role in bone remodelling by promoting bone regeneration through the BMP-2/Smad signaling pathway, clearing infections, and promoting vascular regeneration. Immunohistochemistry was used to examine changes in each indicator in vivo. ALP and BMP-2 (Fig. 10A, B, C), which are key osteogenic indicators, significantly increased at 4w and 8w. The addition of AMPs further enhanced the osteogenic indicators. It was observed that early bacterial clearance significantly promotes osseointegration. CD31 expressions significantly increased in both 4 and 8 weeks, indicating a clear marker of vasculogenesis. To confirm the effect of SV on long-term inflammatory response during macrophage stimulation for MET, the TNF-α factor at the defect site was examined. Local bacterial residues after debridement may cause a local inflammatory response and an increase in the level of TNF-α factor. SV significantly contributes to restoring normal levels of inflammatory factors and decreasing the level of TNF-α factor. Long-term low-dose delivery of SV can effectively prevent the side effects of METs (Fig. 10A–D, E). In the field of osteoimmunology, neutrophils represent the initial line of defence in innate immunity. Neutrophil extracellular traps (NETs) have been demonstrated to kill bacteria. However, research has indicated that an excess of NETs may precipitate adverse effects on the autoimmune system. The role of macrophage extracellular traps (METs) may extend beyond bacterial clearance, encompassing the regulation of NETosis and the remodelling of the immune microenvironment. This includes the modulation of the release of pro- and anti-inflammatory factors. The extent of inflammatory modulation in the late stent phase was demonstrated through vivo experimentation. The exogenous antimicrobial peptide supplementation facilitated rapid clearance of bacteria, reduced NETosis produced to capture bacteria, and prevented a sustained inflammatory response [51].

AMPs act synergistically in the treatment of intracellular infections by macrophages in a two-drug combination system. We established a framework for the surveillance and clearance of intracellular infections, while avoiding adverse effects on osteogenesis through the strategic administration of SVs. SV has been demonstrated to activate immune cells at the defect site for infection management and stimulate osteoblasts for osteogenic mineralization, among other functions. Delivery systems are employed to target osteomyelitis treatment with varying preferences and doses of released drugs. These systems are demonstrated to be instrumental in the treatment of traumatic osteomyelitis after debridement through the prevention of chronic relapsing processes in acute osteomyelitis via long-term management. The observations made in animal experiments at 2, 4, 6, and 8 weeks demonstrated that the composite system was effective in promoting the healing of large bone defects. Additionally, the system was observed to facilitate the clearance of inflammatory cells from the defects.

However, the observations of the system's three-phase process in vivo, which should have included the initiation of composite scaffolds in vivo and the paradigm-shifting process, were limited. Further research is needed to explore the impact of innate immune cells initiation and trapping in osteomyelitis treatment in the future.

4. Conclusion

In this study, we developed a dual-drug reservoir scaffold by incorporating an induced membrane bionic gel bilayer onto 3D-printed PLA-mPEG scaffolds using a layer-by-layer modification strategy. The composite scaffolds simultaneously carried two therapeutic agents—AMPs and simvastatin exhibit distinct release profiles dependent on the architectural configuration of the hierarchical structure and the encapsulation strategy. Dual drug reservoir scaffolds facilitate expeditious bacterial clearance during the initial implantation phase, sustained modulation of macrophage immune responses, and promotion of bone mineralization and regeneration. The composite scaffolds demonstrated excellent antimicrobial efficacy, immune modulation, and osteogenic capacity in both in vitro and in vivo models. Furthermore, the composite scaffolds could prevent graft failure and chronic recurrence of osteomyelitis in the osteomyelitis model established in SD rats, with certain in situ repair capabilities. These findings suggest that this dual-drug reservoir scaffold could provide a promising solution for the treatment of traumatic osteomyelitis and may hold significant potential for clinical applications in bone regeneration and infection management.

CRediT authorship contribution statement

Yutong Zhang: Methodology, Investigation, Conceptualization. **Tongtong Xu:** Supervision, Project administration. **Tieshu Li:** Formal analysis, Data curation. **Hening Chen:** Project administration. **Guangzhe Xu:** Formal analysis. **Wenxin Hu:** Formal analysis. **Yongting Li:** Software. **Yue Dong:** Methodology. **Zhihui Liu:** Writing – review & editing, Supervision, Methodology, Funding acquisition, Conceptualization. **Bing Han:** Writing – review & editing, Methodology, Funding acquisition.

Funding

This research was supported by Jilin Provincial Science and Technology Department of Science and Technology Development Project [Grant No. 20210204016YY].

Declaration of competing interest

The authors declare that they have no known competing financial interests or personal relationships that could have appeared to influence the work reported in this paper.

Appendix A. Supplementary data

Supplementary data to this article can be found online at https://doi.org/10.1016/j.mtbio.2024.101356.

Data availability

Data will be made available on request.

References

[1] Y. Zhao, H. Kang, Y. Xia, L. Sun, F. Li, H. Dai, 3D Printed photothermal scaffold sandwiching bacteria inside and outside improves the infected microenvironment and repairs bone defects, Adv. Healthcare Mater. 13 (2024) e2302879, https://doi.org/10.1002/adhm.202302879.

[2] Y. Ren, L. Liu, D. Sun, Z. Zhang, M. Li, X. Lan, J. Ni, M.-M. Yan, W. Huang, Z.-M. Liu, Aq Peng, Y. Zhang, N. Jiang, K. Song, Z. Huang, Q. Bi, J. Zhang, Q. Yang, J. Yang, Y. Liu, W. Fu, X. Tian, Y. Wang, W. Zhong, X. Song, A. Abudurexiti, Z. Xia, Q. Jiang, H. Shi, X. Liu, G. Wang, Y. Hu, Y. Zhang, G. Yin, J. Fan, S. Feng, X. Zhou, Z. Li, W. He, J. Weeks, E.M. Schwarz, S.L. Kates, L. Huang, Y. Chai, M. Bin Yu, Z. Xie, Z. Deng, C. Xie, Epidemiological updates of post-traumatic related limb osteomyelitis in China: a 10 years multicentre cohort study, Int. J. Surg. 109 (2023) 2721–2731, https://doi.org/10.1097/JS9.0000000000000502.

[3] L.O. Conterno, M.D. Turchi, Antibiotics for treating chronic osteomyelitis in adults, Cochrane Database Syst. Rev. (2013), https://doi.org/10.1002/14651858.CD004439.pub3.

[4] S.S. Sahu, P. Sarkar, S. Shrivastava, A. Chattopadhyay, Differential effects of simvastatin on membrane organization and dynamics in varying phases, Chem. Phys. Lipids 225 (2019) 104831, https://doi.org/10.1016/j.chemphyslip.2019.104831.

[5] G.V. Haute, C. Luft, L. Pedrazza, G.L. Antunes, J. Silveira, B. de Souza Basso, V.G. S. Levorse, M.S. Bastos, D. Melo, K.F. Rodrigues, M.C. Garcia, M.S. da Costa, L. S. Matzenbacher, D.B. Kaiber, M.V.F. Donadio, J. Gracia-Sancho, J.R. de Oliveira, Simvastatin attenuates inflammatory process on LPS-induced acute lung injury in mice, Respir. Physiol. Neurobiol. 309 (2023) 104002, https://doi.org/10.1016/j.resp.2022.104002.

[6] T. Sun, J. Huang, W. Zhang, X. Zheng, H. Wang, J. Liu, H. Leng, W. Yuan, C. Song, Simvastatin-hydroxyapatite coatings prevent biofilm formation and improve bone formation in implant-associated infections, Bioact. Mater. 21 (2022) 44–56, https://doi.org/10.1016/j.bioactmat.2022.07.028.
[7] O.A. Chow, M. von Köckritz-Blickwede, A.T. Bright, M.E. Hensler, A. S. Zinkernagel, A.L. Cogen, R.L. Gallo, M. Monestier, Y. Wang, C.K. Glass, V. Nizet, Statins enhance formation of phagocyte extracellular traps, Cell Host Microbe 8 (2010) 445–454, https://doi.org/10.1016/j.chom.2010.10.005.
[8] C. Wang, T. Hong, P. Cui, J. Wang, J. Xia, Antimicrobial peptides towards clinical application: delivery and formulation, Adv. Drug Deliv. Rev. 175 (2021) 113818, https://doi.org/10.1016/j.addr.2021.05.028.
[9] R. He, J. Sui, G. Wang, Y. Wang, K. Xu, S. Qin, S. Xu, F. Ji, H. Zhang, Polydopamine and hyaluronic acid immobilisation on vancomycin-loaded titanium nanotube for prophylaxis of implant infections, Colloids Surf. B Biointerfaces 216 (2022) 112582, https://doi.org/10.1016/j.colsurfb.2022.112582.
[10] M. Cuvillier, J.-F. Meucci, C. Cazorla, A. Carricajo, T. Neri, B. Boyer, Masquelet's induced membrane technique associated with Reamer Irrigation Aspiration grafting and intramedullary Nailing (MaRIAN) for chronic diaphyseal osteomyelitis of the lower limb, Orthop Traumatol Surg Res 108 (2022) 103395, https://doi.org/10.1016/j.otsr.2022.103395.
[11] B. Jia, Z. Zhang, Y. Zhuang, H. Yang, Y. Han, Q. Wu, X. Jia, Y. Yin, X. Qu, Y. Zheng, K. Dai, High-strength biodegradable zinc alloy implants with antibacterial and osteogenic properties for the treatment of MRSA-induced rat osteomyelitis, Biomaterials 287 (2022) 121663, https://doi.org/10.1016/j.biomaterials.2022.121663.
[12] C. Wang, Y. Lin, J. Huang, H. Song, Y. Zhang, Y. Zhang, M. Xu, J. Liu, Pseudomonas aeruginosa targeting cascade photodynamic nanoassemblies for efficient antibacterial and anti-inflammatory therapy, Nano Today 51 (2023) 101892, https://doi.org/10.1016/j.nantod.2023.101892.
[13] N. Kavanagh, E.J. Ryan, A. Widaa, G. Sexton, J. Fennell, S. O'Rourke, K.C. Cahill, C.J. Kearney, F.J. O'Brien, S.W. Kerrigan, Staphylococcal osteomyelitis: disease progression, treatment challenges, and future directions, Clin. Microbiol. Rev. 31 (2018) e00084, https://doi.org/10.1128/CMR.00084-17, 17.
[14] J. Chen, Y. Li, S. Liu, Y. Du, S. Zhang, J. Wang, Freeze-casting osteochondral scaffolds: the presence of a nutrient-permeable film between the bone and cartilage defect reduces cartilage regeneration, Acta Biomater. 154 (2022) 168–179, https://doi.org/10.1016/j.actbio.2022.09.069.
[15] Y. Chen, Z. Liu, Z. Lin, M. Lu, Y. Fu, G. Liu, B. Yu, The effect of Staphylococcus aureus on innate and adaptive immunity and potential immunotherapy for S. aureus-induced osteomyelitis, Front. Immunol. 14 (2023) 1219895, https://doi.org/10.3389/fimmu.2023.1219895.
[16] K.H. Rasmussen, C.L. Hawkins, Role of macrophage extracellular traps in innate immunity and inflammatory disease, Biochem. Soc. Trans. 50 (2022) 21–32, https://doi.org/10.1042/BST20210962.
[17] R.S. Doster, L.M. Rogers, J.A. Gaddy, D.M. Aronoff, Macrophage extracellular traps: a scoping review, J. Innate Immun. 10 (2018) 3–13, https://doi.org/10.1159/000480373.
[18] C. Garzoni, W.L. Kelley, Return of the Trojan horse: intracellular phenotype switching and immune evasion by Staphylococcus aureus, EMBO Mol. Med. 3 (2011) 115–117, https://doi.org/10.1002/emmm.201100123.
[19] X. Jing, C. Xu, W. Su, Q. Ding, B. Ye, Y. Su, K. Yu, L. Zeng, X. Yang, Y. Qu, K. Chen, T. Sun, Z. Luo, X. Guo, Photosensitive and conductive hydrogel induced innerved bone regeneration for infected bone defect repair, Adv. Healthcare Mater. 12 (2023) 2201349, https://doi.org/10.1002/adhm.202201349.
[20] T. Xu, S. Gao, N. Yang, Q. Zhao, Y. Zhang, T. Li, Z. Liu, B. Han, A personalized biomimetic dual-drug delivery system via controlled release of PTH1-34 and simvastatin for in situ osteoporotic bone regeneration, Front. Bioeng. Biotechnol. 12 (2024) 1355019, https://doi.org/10.3389/fbioe.2024.1355019.
[21] Y. Ren, P. Sikder, B. Lin, S.B. Bhaduri, Microwave assisted coating of bioactive amorphous magnesium phosphate (AMP) on polyetheretherketone (PEEK), Mater. Sci. Eng. C 85 (2018) 107–113, https://doi.org/10.1016/j.msec.2017.12.025.
[22] S. Liu, Y. Zhao, M. Li, L. Nie, Q. Wei, O.V. Okoro, H. Jafari, S. Wang, J. Deng, J. Chen, A. Shavandi, L. Fan, Bioactive wound dressing based on decellularized tendon and GelMA with incorporation of PDA-loaded asiaticoside nanoparticles for scarless wound healing, Chem. Eng. J. 466 (2023) 143016, https://doi.org/10.1016/j.cej.2023.143016.
[23] W. Liu, C. Liu, C. Liu, Y. Li, L. Pan, J. Wang, X. Jian, Surface chemical modification of poly(phthalazinone ether nitrile ketone) through rhBMP-2 and antimicrobial peptide conjugation for enhanced osteogenic and antibacterial activities in vitro and in vivo, Chem. Eng. J. 424 (2021) 130321, https://doi.org/10.1016/j.cej.2021.130321.
[24] R. Chen, T. Feng, S. Cheng, M. Chen, Y. Li, Z. Yu, Z. Xu, P. Yin, L. Zhang, P. Tang, Evaluating the defect targeting effects and osteogenesis promoting capacity of exosomes from 2D- and 3D-cultured human adipose-derived stem cells, Nano Today 49 (2023) 101789, https://doi.org/10.1016/j.nantod.2023.101789.
[25] J. He, P. Ran, M. Chen, W. Cao, S. Xie, G. Zhang, X. Li, Intracellular infection-responsive release of NO and peptides for synergistic bacterial eradication, J. Contr. Release 352 (2022) 87–97, https://doi.org/10.1016/j.jconrel.2022.10.015.
[26] L. Tao, Y. Gao, Y. Li, L. Yang, J. Yao, H. Huang, J. Yu, B. Han, B. Wang, Z. Liu, The preventive effect of photocrosslinked Hep/GelMA hydrogel loaded with PRF on MRONJ, BMC Oral Health 24 (2024) 1010, https://doi.org/10.1186/s12903-024-04792-8.
[27] X. Farto-Vaamonde, L. Diaz-Gomez, A. Parga, A. Otero, A. Concheiro, C. Alvarez-Lorenzo, Perimeter and carvacrol-loading regulate angiogenesis and biofilm growth in 3D printed PLA scaffolds, J. Contr. Release 352 (2022) 776–792, https://doi.org/10.1016/j.jconrel.2022.10.060.
[28] R. Baptista, M. Guedes, Morphological and mechanical characterization of 3D printed PLA scaffolds with controlled porosity for trabecular bone tissue replacement, Mater. Sci. Eng. C 118 (2021) 111528, https://doi.org/10.1016/j.msec.2020.111528.
[29] S. Salehi, H. Ghomi, S.A. Hassanzadeh-Tabrizi, N. Koupaei, M. Khodaei, The effect of polyethylene glycol on printability, physical and mechanical properties and osteogenic potential of 3D-printed poly (l-lactic acid)/polyethylene glycol scaffold for bone tissue engineering, Int. J. Biol. Macromol. 221 (2022) 1325–1334, https://doi.org/10.1016/j.ijbiomac.2022.09.027.
[30] H. Chinnasami, M.K. Dey, R. Devireddy, Three-dimensional scaffolds for bone tissue engineering, Bioengineering (Basel) 10 (2023) 759, https://doi.org/10.3390/bioengineering10070759.
[31] M. Hossein, A. Baidya, R. Haghniaz, E. Davoodi, S. Ahadian, N. Annabi, A. Khademhosseini, P.S. Weiss, Stretchable and bioadhesive gelatin methacryloyl-based hydrogels enabled by *in situ* dopamine polymerization, ACS Appl. Mater. Interfaces 13 (2021) 40290–40301, https://doi.org/10.1021/acsami.1c10048.
[32] S. Hu, X. Pei, L. Duan, Z. Zhu, Y. Liu, J. Chen, T. Chen, P. Ji, Q. Wan, J. Wang, A mussel-inspired film for adhesion to wet buccal tissue and efficient buccal drug delivery, Nat. Commun. 12 (2021) 1689, https://doi.org/10.1038/s41467-021-21989-5.
[33] Y. Yuan, Q. Xue, Q. Guo, G. Wang, S. Yan, Y. Wu, L. Li, X. Zhang, B. Li, The covalent crosslinking of dialdehyde glucomannan and the inclusion of tannic acid synergistically improved physicochemical and functional properties of gelatin films, Food Packag. Shelf Life 30 (2021) 100747, https://doi.org/10.1016/j.fpsl.2021.100747.
[34] X. Chen, Y. Zhang, W. Yu, W. Zhang, H. Tang, W.-E. Yuan, In situ forming ROS-scavenging hybrid hydrogel loaded with polydopamine-modified fullerene nanocomposites for promoting skin wound healing, J. Nanobiotechnol. 21 (2023) 129, https://doi.org/10.1186/s12951-023-01879-2.
[35] A. Jin, Y. Wang, K. Lin, L. Jiang, Nanoparticles modified by polydopamine: working as "drug" carriers, Bioact. Mater. 5 (2020) 522–541, https://doi.org/10.1016/j.bioactmat.2020.04.003.
[36] S. Lappe, D. Mulac, K. Langer, Polymeric nanoparticles – influence of the glass transition temperature on drug release, Int. J. Pharm. 517 (2017) 338–347, https://doi.org/10.1016/j.ijpharm.2016.12.025.
[37] X. Gao, J. Ding, C. Liao, J. Xu, X. Liu, W. Lu, Defensins: the natural peptide antibiotic, Adv. Drug Deliv. Rev. 179 (2021) 114008, https://doi.org/10.1016/j.addr.2021.114008.
[38] Hyaluronic acid-based hydrogel coatings on Ti6Al4V implantable biomaterial with multifunctional antibacterial activity, Carbohydr. Polym. 301 (2023) 120366, https://doi.org/10.1016/j.carbpol.2022.120366.
[39] R. García-Alvarez, I. Izquierdo-Barba, M. Vallet-Regí, 3D scaffold with effective multidrug sequential release against bacteria biofilm, Acta Biomater. 49 (2017) 113–126, https://doi.org/10.1016/j.actbio.2016.11.028.
[40] M.J. Dewey, A.J. Collins, A. Tiffany, V.R. Barnhouse, C. Lu, V. Kolliopoulos, I. Mutreja, N.J. Hickok, B.A.C. Harley, Evaluation of bacterial attachment on mineralized collagen scaffolds and addition of manuka honey to increase mesenchymal stem cell osteogenesis, Biomaterials 294 (2023) 122015, https://doi.org/10.1016/j.biomaterials.2023.122015.
[41] W. Liu, X. Dan, W.W. Lu, X. Zhao, C. Ruan, T. Wang, X. Cui, X. Zhai, Y. Ma, D. Wang, W. Huang, H. Pan, Spatial distribution of biomaterial microenvironment pH and its modulatory effect on osteoclasts at the early stage of bone defect regeneration, ACS Appl. Mater. Interfaces 11 (2019) 9557–9572, https://doi.org/10.1021/acsami.8b20580.
[42] T. Sun, J. Huang, W. Zhang, X. Zheng, H. Wang, J. Liu, H. Leng, W. Yuan, C. Song, Simvastatin-hydroxyapatite coatings prevent biofilm formation and improve bone formation in implant-associated infections, Bioact. Mater. 21 (2022) 44–56, https://doi.org/10.1016/j.bioactmat.2022.07.028.
[43] A. Salhotra, H.N. Shah, B. Levi, M.T. Longaker, Mechanisms of bone development and repair, Nat. Rev. Mol. Cell Biol. 21 (2020) 696–711, https://doi.org/10.1038/s41580-020-00279-w.
[44] J. Li, J. Ma, H. Sun, M. Yu, H. Wang, Q. Meng, Z. Li, D. Liu, J. Bai, G. Liu, X. Xing, F. Han, B. Li, Transformation of arginine into zero-dimensional nanomaterial endows the material with antibacterial and osteoinductive activity, Sci. Adv. 9 (2023) eadf8645, https://doi.org/10.1126/sciadv.adf8645.
[45] R.D.A. Cayetano, G.-B. Kim, J. Park, Y.-H. Yang, B.-H. Jeon, M. Jang, S.-H. Kim, Biofilm formation as a method of improved treatment during anaerobic digestion of organic matter for biogas recovery, Bioresour. Technol. 344 (2022) 126309, https://doi.org/10.1016/j.biortech.2021.126309.
[46] C.W. Hall, T.-F. Mah, Molecular mechanisms of biofilm-based antibiotic resistance and tolerance in pathogenic bacteria, FEMS Microbiol. Rev. 41 (2017) 276–301, https://doi.org/10.1093/femsre/fux010.
[47] E.A. Masters, B.F. Ricciardi, K.L. de M. Bentley, T.F. Moriarty, E.M. Schwarz, G. Muthukrishnan, Skeletal infections: microbial pathogenesis, immunity and clinical management, Nat. Rev. Microbiol. 20 (2022) 385–400, https://doi.org/10.1038/s41579-022-00686-0.
[48] T.M. Koushik, C.M. Miller, E. Antunes, Bone tissue engineering scaffolds: function of multi-material hierarchically structured scaffolds, Adv. Healthcare Mater. 12 (2023) e2202766, https://doi.org/10.1002/adhm.202202766.
[49] R. Nie, Y. Sun, H. Lv, M. Lu, H. Huangfu, Y. Li, Y. Zhang, D. Wang, L. Wang, Y. Zhou, 3D printing of MXene composite hydrogel scaffolds for photothermal

antibacterial activity and bone regeneration in infected bone defect models, Nanoscale 14 (2022) 8112–8129, https://doi.org/10.1039/D2NR02176E.

[50] K. Mys, P. Varga, F. Stockmans, B. Gueorguiev, C.E. Wyers, J.P.W. van den Bergh, G.H. van Lenthe, Quantification of 3D microstructural parameters of trabecular bone is affected by the analysis software, Bone 142 (2021) 115653, https://doi.org/10.1016/j.bone.2020.115653.

[51] D. Nakazawa, H. Shida, Y. Kusunoki, A. Miyoshi, S. Nishio, U. Tomaru, T. Atsumi, A. Ishizu, The responses of macrophages in interaction with neutrophils that undergo NETosis, J. Autoimmun. 67 (2016) 19–28, https://doi.org/10.1016/j.jaut.2015.08.018.